GRAIN-SCALE COMMINUTION AND ALTERATION OF ARKOSIC ROCKS IN THE DAMAGE ZONE OF THE SAN ANDREAS FAULT AT SAFOD

A Thesis

by

BRETANI REBECCA HERON

Submitted to the Office of Graduate Studies of
Texas A&M University
in partial fulfillment of the requirements for the degree of

MASTER OF SCIENCE

December 2011

Major Subject: Geology

Grain-scale Comminution and Alteration of Arkosic Rocks in the Damage Zone of the San Andreas Fault at SAFOD

GRAIN-SCALE COMMINUTION AND ALTERATION OF ARKOSIC ROCKS IN THE DAMAGE ZONE OF THE SAN ANDREAS FAULT AT SAFOD

A Thesis

by

BRETANI REBECCA HERON

Submitted to the Office of Graduate Studies of
Texas A&M University
in partial fulfillment of the requirements for the degree of

MASTER OF SCIENCE

Approved by:

Co-Chairs of Committee,	Judith Chester
	Frederick Chester
Committee Member,	Giovanna Biscontin
Head of Department,	Andreas Kronenberg

December 2011

Major Subject: Geology

ABSTRACT

Grain-scale Comminution and Alteration of Arkosic Rocks in the Damage Zone of the San Andreas Fault at SAFOD. (December 2011)

Bretani Rebecca Heron, B.S., The University of Texas at Austin

Co-Chairs of Advisory Committee: Dr. Judith Chester
Dr. Frederick Chester

Spot core from the San Andreas Fault Observatory at Depth (SAFOD) borehole provides the opportunity to characterize and quantify damage and mineral alteration of siliciclastics within an active, large-displacement plate-boundary fault zone. Deformed arkosic, coarse-grained, pebbly sandstone, and fine-grained sandstone and siltstone retrieved from 2.55 km depth represent the western damaged zone of the San Andreas Fault, approximately 130 m west of the Southwest Deforming Zone (SDZ). The sandstone is cut by numerous subsidiary faults that display extensive evidence of repeating episodes of compaction, shear, dilation, and cementation. The cataclasites contain fractured host-rock particles of quartz, oligoclase, and orthoclase, in addition to albite and laumontite produced by syn-deformation alteration reactions. This study quantifies the particle size distributions and the particle shape of the host rock mineral phases and the volume fraction of the alteration products for the following structural units distinguished in the subsidiary fault zones: fractured sandstones, brecciated sandstones, microbreccias, microbreccias within distinct shear zones, and principal slip surfaces. Overall, the particle sizes are consistent with a power law distribution over the

particle size range investigated (0.3 μm < d < 400 μm). The exponent (fractal dimension, D) is found to increase with shear strain and volume fraction of laumontite. This overall increase in D and evolution of shape with increasing shear strain reflects a general transition from constrained comminution, active at low shear strains to abrasion processes that dominate at high shear strains.

ACKNOWLEDGEMENTS

I would like to thank everyone in the Department of Geology and Geophysics for making my time at Texas A&M truly memorable. Specifically, I would like to thank my committee co-chair, Dr. Judith Chester. She has dedicated abundant time and effort into shaping this project and has provided me with excellent guidance and enthusiasm for this research. Thank you to my other co-chair, Dr. Frederick Chester, for all his assistance and valuable input and committee member, Dr. Giovanna Biscontin, for her support and availability. I would also like to recognize and thank Dr. Ray Guillemette for his help throughout the course of this research and for his sincere desire to teach and share his knowledge. Thank you to Tom Stephens for his help using the SEM.

I would also like to thank all of my friends in the Center for Tectonophysics. Sean and Jennifer, I am so thankful for your friendship and support and for the countless memories. Alphie, you have been such a great friend and positive influence in my life. Fatih, you are a wonderful person and friend. I believe you can do anything you set your mind to do. I also want to extend my gratitude to the National Science Foundation and Earthscope for providing the funding for this project.

Thanks to my family for their endless support and love. I wouldn't be where I am today without you. I am truly blessed. Stephen, you are the best brother. Thank you so much for all of your help.

Finally, I would like to thank my boyfriend, Austin. You have helped me more than you know. I could never have done this without you. I love you.

TABLE OF CONTENTS

Page

LIST OF FIGURES

FIGURE Page

LIST OF TABLES

1. INTRODUCTION

Major plate-boundary faults in the continental crust often consist of one or more fault cores that are bounded by zones of associated damage [e.g., *Sibson*, 1986; *Chester et al.*, 1993; *Wibberley and Shimamoto*, 2003; *Chester et al.*, 2004; *Imber et al.*, 2008; *Savage and Brodsky*, 2011]. Fault cores represent the zones of highly concentrated fault-parallel shear, and can display distinct layers representing different degrees of strain localization and different magnitudes of displacement. In many studies these regions are referred to as the "on-fault" zones, as they serve as long-standing sites of recurrent rupture or zones of persistent fault-creep [*Sibson*, 2003]. The surrounding damage zones are cut by subsidiary faults and fractures of all scales, and although these zones accommodate much less shear strain than the cores, the deformation in the damage zone is integral to fault formation, accommodation of slip in the core, and the mechanics of faulting [e.g., *Scholz et al.*, 1993; *Chester et al.*, 2004]. In the case of earthquake faulting, the "off-fault" deformation in the damage zone plays an important role in energy dissipation, influences dynamic rupture characteristics, and accounts for a significant portion of the total earthquake energy budget [e.g., *Andrews*, 2005; *Chester et al.*, 2005; *Templeton and Rice*, 2008].

Spot core from the San Andreas Fault Observatory at Depth (SAFOD) borehole (Figure 1) [e.g., *Zoback et al.*, 2011] provides the unique opportunity to characterize and quantify the in situ damage and mineral alteration of siliciclastics along an active, large-

---

This thesis follows the style of *Journal of Geophysical Research.*

displacement, plate-boundary fault zone currently undergoing seismic and aseismic slip. Such data are critical to define how the porosity, permeability, and strength of a fault zone evolve spatially and temporally, and can help constrain estimates of the energetics of earthquake rupture events [e.g., *Kanamori*, 1994; *Wibberley and Shimamoto*, 2003; *Chester et al.*, 2005; *Faulkner et al.*, 2011].

Twelve meters of deformed arkosic, coarse-grained, pebbly sandstone, and fine-grained sandstone and siltstone were retrieved during Phase 1 drilling at SAFOD. These samples represent the westernmost portion of the damage zone [*Chester et al.*, 2007; *Heron et al.*, 2011] of the San Andreas Fault (SAF) at 2.55 km depth and 130 m west of the actively creeping Southwest Deforming Zone (SDZ) (Figure 2) [*Zoback et al*., 2010]. We hypothesize that the deformation displayed in this core represents the cumulative damage suffered by the western wall rock as it was transported 315 km to the northwest from the seismogenic section of the SAF to its current location adjacent the southern end of the creeping section. If correct, the deformation features present can provide a record of the off-fault damage produced during a long history of coseismic slip and interseismic creep, and of damage recovery by a number of healing processes.

The goal of this study is to quantify the microstructural characteristics of particles in representative subsidiary faults cutting the arkosic sandstone in the western damage zone to determine the role of cataclasis, dissolution, and neomineralization during the earthquake cycle and better understand the origin of off-fault damage and the earthquake energy budget.

2. BACKGROUND

During an earthquake rupture event, radiated energy is released in the form of seismic waves generating potentially destructive ground motion, the quantification of which is crucial to sound earthquake hazard assessment. Estimating the magnitude of radiated energy requires multiple assumptions and leaves a large margin of error [*Kanamori*, 2004]. The energy available for radiation as seismic waves can be determined from the total earthquake energy budget that, to first order, defines the transformation of the elastic strain energy to radiated energy, fracture energy, and frictional heat [*Kanamori*, 2004]. The latter two terms can be constrained to some extent by quantifying fracture and frictional energy within the core and damage zone of an active fault [e.g., *Chester et al.*, 2005; *Wilson et al.*, 2005; *Ma and Archuleta*, 2006]. Detailed meso- and micro-structural characterization of the entire fault zone is required to estimate these parameters. The evolution of cataclastic fault rock textures within the fault zone by fragmentation, grinding, and compaction [e.g., *Storti et al.*, 2003] results in grain shape and size data that can provide critical information needed to constrain the timing and magnitude of fracture and friction energy of the earthquake budget. One key component of this characterization is an estimate of the total surface area of all fractured grains within the subsidiary faults cutting the damage zone [e.g., *Chester et al.*, 2005].

Total fracture surface area has been estimated from PSDs, often with the assumption that all grain surfaces in fault gouge represent brittle failure associated with earthquake rupture events at low temperature and pressure conditions and moderately

high strain rates [e.g., *Sibson*, 1977; *Biegel and Sammis*, 2004; *Chester et al.*, 2005; *Wilson et al.*, 2005]. The size and shape of particles in fault rocks, however, also can reflect interseismic processes including subcritical cracking, neomineralization, and mineral alteration resulting from fluid-rock reactions [e.g., *Evans and Chester*, 1995]. Chemical and physical changes that occur during interseismic periods should not be included in estimates of fracture surface energy associated with the breakdown in strength during rupture [*Kanamori*, 2004; *Chester et al.*, 2005; *Tinti et al.*, 2005].

Numerous previous studies have measured and analyzed PSDs and the shapes of grains of natural fault rocks and of rocks deformed in the laboratory [e.g., *Engelder*, 1974; *Olgaard and Brace*, 1983; *Sammis et al.*, 1987; *Biegel et al.*, 1989; *Marone and Scholz*, 1989; *Blenkinsop*, 1991; *An and Sammis*, 1994; *Mair*, 2002; *Storti et al.*, 2003; *Heilbronner and Keulen*, 2006; *Billi*, 2007; *Keulen et al.*, 2007; *Bjørk et al.*, 2009]. Many of these studies observe that for a limited range of grain sizes, particles display a fractal geometry [*Mandelbrot*, 1982] and are best described by a power law relationship

$$N(S) \approx S^{-n}, \tag{1}$$

where $N(S)$ represents the number of particles of size S, and n is related to the fractal dimension. In (1), the value of n depends on the type of distribution (i.e., frequency, density, or cumulative) and how the data are binned (i.e., linear or logarithmic) [*Bonnet et al.*, 2001]. For a cumulative distribution, (1) may be written as

$$C(d) = ad^{-D}, \quad (2)$$

where $C(d)$ is the cumulative number of particles greater than size d, a is a constant, and the exponent, D, is equal to the fractal dimension. From measurements of particle size, D may be determined from the slope of the best-fit line to data plotted as log $C(d)$ versus log d [e.g., *Sammis and Biegel*, 1989; *Blenkinsop*, 1991; *Turcotte*, 1992; *Bonnet et al.*, 2001; *Storti et al.*, 2003]. The fractal dimension (D) may be used to compare PSDs determined by different methods and in different topological dimensions, and to interpret the fragmentation processes [e.g., *Marone and Scholz*, 1989; *Sammis and Biegel*, 1989; *Blenkinsop*, 1991].

Several different methods have been employed to measure PSDs, including the automated technique using a laser particle analyzer and the traditional pipette-sieve method using a pipette rack [*Sammis et al.*, 1986; *Billi*, 2004; *Wilson et al.*, 2005; *Rockwell et al.*, 2009]. These techniques are best suited for 3-D characterizations of naturally disaggregated materials and for loosely or poorly cemented materials, and can be used to measure particles ranging in size from 0.07 mm to greater than 1 cm. Measurement of particles less than 0.07 mm in diameter may result in biased data because of bonding effects between small particles [*Krumbein and Pettijohn*, 1990; *Billi*, 2007; *Rockwell et al.*, 2009]. Primary disadvantages associated with the sieve technique are that 1) spatial relationships are lost along with any information that these relationships could provide, and 2) for cohesive materials there is the expectation that

disaggregation will be incomplete or create artificial fracture surfaces [*Sammis et al.*, 1987].

For cohesive rocks, analysis of 2-D images is the technique of choice [*Sammis et al.*, 1986; *Billi*, 2004; *Heilbronner and Keulen*, 2006; *Rockwell et al.*, 2009]. Image analysis techniques maintain geometrical and spatial relationships and may also be used to explore particle shape and surface topography [e.g., *Storti et al.*, 2007]. One disadvantage of the 2-D imaging technique is the possible misrepresentation of large particles associated with the limited sample area captured by imaging [*Sammis et al.*, 1987; *Billi*, 2007]. Rawling and Goodwin [2003] compare sieve and imaging techniques for disaggregated materials and explain that the sieve method, as a first order approximation, measures intermediate particle axes, whereas imaging methods measure both intermediate and long axis dimensions and thus gives more information about particle size. An additional problem associated with measurements made from random 2-D slices through solids is that most particles are sliced off-center and thus the analysis of images tends to underestimate particle dimensions, and that there is a greater probability of intersecting large particles, causing an underrepresentation of the small particle size fraction [e.g., *Blenkinsop*, 1991]. It is possible to correct for these effects, particularly if particles tend toward spherical shapes [*Underwood*, 1968; *Exner*, 1972; *Falconer*, 1985; *Sammis et al.*, 1987].

The value of D depends on the topological dimension of the measurement, i.e., volume- or mass-based determinations (e.g., sieving) result in larger values of D when compared with area-based determinations (e.g., image slices). Based on the fractal

theory defined by Falconer [1985], most conclude that if particles tend towards spherical shapes then the volume-based *D* is greater than the area-based *D* by a value of 1 [*Sammis et al*., 1987]. We follow this rule to convert reported values of D between topological dimensions, and in this paper all values of D are given in terms of a topological dimension of 2.

3. GEOLOGICAL OBSERVATIONS

3.1. Geology of the San Andreas Fault at SAFOD

The SAF is an active, right-lateral continental transform fault that forms the active boundary between the North American and Pacific plates [*Catchings et al.*, 2002]. SAFOD is located at the southernmost portion of the central creeping (aseismic) zone, just northwest of the Parkfield segment (Figure 1). At this location, displacement on the fault primarily occurs by aseismic creep and repeating microseismic events. Seven M6 earthquakes have occurred on the Parkfield segment since 1857; the most recent taking place in 2004 [*Zoback et al.*, 2011]. The SAF juxtaposes Cretaceous granitic rocks of the Salinian block on the southwest, and Jurassic through Cretaceous rocks of the Franciscan complex and Great Valley Sequence on the northeast, throughout most of central California. Tertiary through Pleistocene sedimentary rocks locally cover the Salinian rocks in the vicinity of SAFOD [*Dickinson*, 1966; *Page*, 1981; *Kistler and Champion*, 1986; *Catchings* et al., 2002; *Blythe et al.*, 2004; *McPhee et al.*, 2004]. The Salinian rocks were transported along the fault approximately 300 km from their place of origin as part of the southern Sierra Nevada batholith [e.g., *Blythe et al.*, 2004; *McPhee et al.*, 2004]. In the vicinity of SAFOD, the fault zone is approximately 5km wide at depth and is composed of several subparallel fault traces [e.g., *Rymer et al.*, 2003].

Phase 1 of the SAFOD borehole penetrated Tertiary sediments overlying the Salinian granite in the vertical portion of the borehole. At ~1.5 km depth, the borehole was deviated 59 degrees from vertical and crossed the Buzzard Canyon Fault, a large

subsidiary fault of the San Andreas system that places Salinian granite against arkosic sedimentary rocks. Cuttings recovered when the borehole was extended, during Phase 2 drilling, indicate that the arkosic sedimentary sequence extends to 3157 m MD. At this location it is juxtaposed against fine-grain sandstones and mudstones of the Cretaceous Great Valley Sequence (Figure 2). This change in lithology marks the boundary between terranes associated with the Pacific and North American plates in central California [*Zoback et al.*, 2011]. The age and origin of the arkosic sedimentary rocks is uncertain, but Draper-Springer et al. [2009] suggest that they are Cretaceous to early Eocene fluvial or marine fans that were sourced by Salinian granitic terrains [*Clarke and Nilsen*, 1973; *Graham*, 1978]. They were transported north to their current location by slip on the Buzzard Canyon Fault and the modern day SAF.

3.2. Sample Description

The arkosic sandstone and siltstone recovered from 2680-3156 m MD contains 30-60% quartz, 10-40% feldspar (equal amounts of plagioclase and orthoclase), minor amounts of chlorite, and a greater percentage of illite and laumontite when compared to the shallower arkosic sandstone unit at 1920 to 2530 m MD [*Solum et al.*, 2006; *Bradbury et al.*, 2007; *Draper-Springer et al.*, 2009].

This study focuses on the massively bedded, well-cemented, coarse-grained arkosic sandstone section between 3056 and 3062 m MD. This section contains pebble size fragments of granite, sandstone, siltstone, and volcanic clasts, and a few cobble size-clasts. A minor cataclastic fault at approximately 3062 m MD marks the abrupt

transition from the coarse-grain sandstone to the fine-grain siltstone found at greater depths. The sandstone is cut by numerous mesoscale subsidiary faults, including cataclastic shear bands ($\leq$ 2 cm thick) that are oriented at high angles to the core axis, and network of millimeter-thick shear fractures that form a conjugate fracture set. This fracture set is defined by a shortening direction that is sub-parallel to the borehole axis and therefore is roughly orthogonal to the SAF (132°, 83° SW) at SAFOD (Figure 3) [*Almeida*, 2007].

For this microstructural analysis, the subsidiary faults are grouped into three size-classes: 1) small faults, 1 to 2 mm thick, that record an early stage of fault development, 2) intermediate-size faults, 2 to 3 mm thick, that show cataclastic grain size reduction and flow, extensive cementation, and alteration of host particles, and 3) large subsidiary faults that have cemented cataclastic zones up to 10 mm thick. We assume that fault thickness scales with fault displacement [*Scholz*, 1987], so the smallest faults have displacments on the order of a centimeter and the particle sizes and shapes represent those produced at the earliest stages of fault development. The thickest faults have displacements on the order of several decimeters and represent more mature subsidiary faults. For each size-class of faults, one representative subsidiary fault was sampled from the spot core and sectioned for study (Figure 4). Each petrographic section is oriented perpendicular to the fault plane and approximately parallel to the shear direction.

3.3. Microstructural Observations

On the basis of microstructures, five distinct structural units are distinguished in the subsidiary fault zones: fractured sandstone (FSS), brecciated sandstone (BSS), microbreccia (MB), microbreccia within a distinct shear zone (MBS), and principal slip zone (PSZ) (Figures 4 and 5a). Seven regions representing the BSS, MB, and MSB are studied in detail. The FSS and PSZ units will be analyzed in a future study. The large subsidiary fault is subdivided into sub-regions, each representing a distinct structural unit (Figure 5b and c).

The FSS unit represents the moderately fractured arkosic sandstone host rock. It is composed of the original coarse-grains (<1-5 mm) of quartz, oligoclase, and orthoclase, and some alteration products including albite, laumontite, and calcite. The albite, laumontite, and calcite are the products of laumontization and albitization [e.g., *Boles and Coombs*, 1977; *Boles*, 1982; Blenkinsop and Sibson, 1992]. Grain boundary, intragranular, and transgranular microfractures are present. The fractures are open, partially or completely sealed with quartz or other phases, or are healed (i.e., display fluid inclusion planes). Transgranular fractures cut across several grains and are oriented approximately sub-parallel and sub-normal to the fault zone [*Almeida*, 2007]. Quartz grains often exhibit undulose extinction, and are cut by open, sealed and healed fractures. The most common fracture-fill is laumontite. The orthoclase primarily is microcline in composition, as evidenced by the presence of tartan twinning [*Draper-Springer et al.*, 2009]. This phase is relatively unaltered, displaying minor illite

replacement, and fractures primarily occur along cleavage. The surviving oligoclase grains are partially altered to albite, and less commonly, to muscovite.

The BSS and MB structural units are similar to the FSS unit; however, alteration of oligoclase is more extensive, there is a greater percentage of laumontite and albite, and the fracture intensity progressively increases, as reflected by a greater reduction in particle size (Figure 6). Fracture intensity is greatest in the feldspar grains, which exhibit smaller particle sizes and more alteration than the quartz particles. Orthoclase alteration includes minor albite intergrowths, minor albite alteration along cleavage planes, and minor illite replacement. The sub-parallel or sub-normal intragranular fractures extend beyond the length of the thin section and are defined as bands of concentrated iron oxide cement. The sub-angular clasts of the host rock, and of laumontite and albite occur within regions of fine-grained laumontite. These clasts are less than 100 μm to about 3 mm in diameter. The primary difference between the BSS and the MB is an increase in the fine particle size fraction within the MB unit.

MBS units are defined in the large and intermediate subsidiary faults, adjacent the zones of most concentrated shear (i.e., PSZs). The MBS unit represents a region that has undergone extensive shear deformation, experienced a significant reduction in particle size, provides evidence of significant dilation in zones that parallel the PSZ, and extensive cementation by laumontite (Figure 5b and c). Survivor clasts in the MBS, as in the MB unit, are particles of the host-rock and of the alteration reactions, where the largest of these are much smaller than those found in the MB unit, typically being less than 300 μm. Sub-regions representing different structural units included fine-grained

cataclastic zones, and bands of fractured and cataclastic laumontite that surrounds particles of the host-rock and alteration products. In some regions these laumontite zones contain grain fragments that were derived from the walls of the shear zone, and fragments of the same grain that are separated by laumontite, but that do not signs of rotation, similar to those described by Blenkinsop and Sibson [1992]. These latter features suggest significant dilation has occurred. The quartz grains are larger and more angular than particles of orthoclase and oligoclase ($\leq$ 75 μm). Many of the survivor particles are oriented with their long axis parallel to the PSZ.

The PSZ unit is best developed in the large subsidiary fault zone where it is defined by a localized band of extreme particle size reduction that is less than 0.5 mm thick (Figure 5). This narrow zone of sub-micron scale material is characterized by alternating light and dark bands that are sparsely populated with survivor clasts, most of which are quartz. Future work to define the characteristics of this zone will require scanning and transmission electron microscopy to define particle size and shape distributions.

4. PARTICLE SIZE AND SHAPE ANALYSIS METHOD

Using the representative samples of subsidiary faults we quantify the evolution of particle size and shape reduction as a function of shear strain and mineralogy for the main mineral phases (plagioclase, orthoclase, and quartz) using 1) back-scattered electron imaging to distinguish particle size and shape, and elemental mapping to distinguish phases, and 2) a combination of manual and automated image analysis techniques.

4.1. Phase Determination by Element Mapping

In some cases it is possible to distinguish mineral phases through automated image analysis (e.g., SXM, ImageJ, MATLAB) by filtering and thresholding BSE images [e.g., *Heilbronner and Keulen*, 2006; *Keulen et al*., 2007]. The plagioclase, quartz, and laumontite in the SAFOD samples, however, often display a similar range of Z values making automated phase separation unreliable. For this reason, element maps are acquired by wavelength-dispersive X-ray spectroscopy (WDS) on a Cameca SX50 electron microprobe to facilitate mineral identification within the subsidiary faults.

Element mapping involves positioning the wavelength-dispersive spectrometers to measure specific X-ray wavelengths from elements of interest and either moving the stage over a square grid of points (stage scanning), or holding the stage stationary and scanning the beam over a square grid of points (beam scanning) [*Williams et al.*, 2001]. For this study, maps at two scales are collected for the BSS, MB, and MBS structural

units in each fault class when present. Large area maps are either 1 x 1 mm, with a resolution of 512 x 512 pixels (a pixel size of 2 x 2 μm), or 1 x 2 mm, with a resolution of 512 x 1024 pixels. Small area maps are 32 x 32 μm with a resolution of 128 x 128 pixels (a pixel size of 0.25 x 0.25 μm). The large area maps are collected by the stage-scanning technique and the small area maps are collected by the beam-scanning technique. The maps are acquired with a 15 kV, 20 nA beam with a 15 ms count time at each pixel. Si is mapped to resolve quartz; K, Al, and Si are mapped to resolve orthoclase; Na, Al, and Si are mapped to resolve albite; Ca, Al, Na, and Si are mapped to resolve oligoclase; and Ca, Al, and Si are mapped to resolve laumontite. The element maps are stacked using ImageJ to create composite element maps indexed to mineral phases by color (Appendix A).

4.2. Particle Size Analysis

At least three sets of overlapping BSE images (5 to 8 images per set) are taken of each structural unit studied. Images are taken at 50X using a petrographic microscope to analyze the largest particles. To determine the size of smaller particles, BSE images are acquired using a FEI QUANTA A 600 FE scanning electron microscope with a 20 kV acceleration voltage at a scan speed of 0.1ms and total acquisition time of 6.2 min/frame. Additional images in a few regions are collected at a scan speed of 30 μsec (1.8 min/frame). The BSE image sets are taken at four magnifications, each increasing by a factor of 4, starting at 150X and increasing up to 9600X to produce 16 bit images with a resolution of 2048 x 1887 pixels. The image resolution in each set permits significant

image enlargement allowing measurement of particle sizes ranging from 0.2 μm to 400 μm.

The colorized phase map composites are superposed onto the BSE images of the same area to aid in defining particle phases and particle boundaries (Figure 6). Grain boundaries are traced in Adobe Photoshop using a digitizing tablet because, after several trial cases, it was determined that the manual digitization technique is the most expedient way to ensure accurate delineation of all fracture surfaces in the multiphase rocks. BSE images can be enlarged up to 400% before becoming pixelated on most screens, which allows more accurate particle boundary identification. For each set of images, all resolvable particles that are wholly contained within the image composite are traced. The smallest traceable particle size is defined by the BSE limit of resolution for the images acquired at 150, 600, and 2400x, and by the resolution of the phase maps (0.25 mm per pixel) for images taken at 9600x. In the stacked BSE-mineral phase maps, the phase of extremely small particles can be defined if the particle is at least two pixels in size. Spurious x-ray counts that are recorded during element mapping and the uncertainty in aligning the BSE images and phase maps makes phase and particle identification inaccurate for smaller grains. Therefore, in the highly sheared regions where the smallest grains exist, the resolution of the phase maps limit the smallest grain size reported in this study.

To determine the role of mineralogy on PSD and magnitude of strain, the particle sizes of plagioclase, orthoclase, and quartz grains are analyzed separately. An 8-bit, grayscale, binary image of each phase is created. Particle size and shape is determined

from the images using ImageJ (http://rsbweb.nih.gov/ij/). Only grains fully contained within an image composite are analyzed (Appendix B).

ImageJ determines the area, A, of a particle that is calculated from the total number of connected pixels that are in contact by at least one pixel edge or pixel corner. The particle diameter is calculated assuming that the particle shape is a perfectly circular object, such that the equivalent particle diameter, d, is given by $d = \sqrt{(4A/p)}$. The equivalent particle diameter assumption provides an objective and reproducible means to characterize size [e.g., *Bjørk et al.*, 2009]. Figure 7 shows an example of a log *d* versus *C(d)* plot where the PSD data, collected at multiple magnifications, are normalized by area and combined to give a single PSD curve. The particle diameters determined are expressed in millimeters and binned at a log *d* interval of 0.05 mm. The best-fit line to the distribution and fractal dimension, *D,* are shown. The cumulative number of particles (i.e., the number of particles greater than a certain size) at each magnification is normalized by the total image area processed to account for the change in imaged area with a shift in magnification. The *D* is determined after identifying the upper and lower fractal limits.

4.3. Particle Shape Analysis

The shape of particles is quantified in terms of circularity, solidity, and elongation [e.g., Crompton, 2005] using ImageJ (Appendix B). Circularity (*C*) measures the ratio between the perimeter of a circle with the same area as the particle, (P_{EAC}), by the true particle perimeter, (P_P) [*Cromtpon*, 2005; *Bjørk et al.*, 2009], which can be

defined in terms of the equivalent circular area of the particle and the true particle perimeter

$$C = \frac{P_{EAC}}{P_{Particle}} = 2\pi\left(\frac{\sqrt{\frac{A_{Particle}}{\pi}}}{P_{Particle}}\right). \quad (3)$$

Both the overall form and surface roughness influence circularity (Figure 8). Circularity values range from 1.0 for a perfectly smooth circle, to values approaching 0 for extremely irregular, elongate shapes. To calculate particle perimeter, ImageJ employs an algorithm that gives pixel edges a value of 1 and corners a value of $\sqrt{2}$ which produces increasingly inaccurate perimeter measurements as particle size decreases, particularly for particles defined by a small number of pixels. In this study, we noted obvious inaccuracy for particles with d < 5 μm, and thus restrict our analysis to particles greater than or equal to this size.

Solidity (*S*) quantifies the surface roughness of a particle by dividing the particle area by the convex hull area, (A_{CH}),

$$S = \frac{A_{Particle}}{A_{CH}}, \quad (4)$$

where the convex hull area may be envisioned as the area enclosed by an imaginary rubber band that is positioned around the particle [*Cromtpon*, 2005]. A perfectly smooth

particle yields a solidity value of 1.0, which decreases towards 0 with an increase in surface irregularity (Figure 8). Unlike circularity, the solidity value is not affected by the overall form of a particle and is only a measure of the roughness of a granular surface. Bjork et al. [2009] use a similar shape descriptor called convexity to quantify the roughness of particle surfaces. Convexity is measurement of the ratio of the convex perimeter (perimeter of rubber band enclosing the particle) to the particle perimeter. When compared to solidity, convexity is more sensitive to the depth and width of the surface indentions. For example, deep, narrow indentions do not change particle area significantly, but have a significant influence on the particle perimeter, and therefore on the convexity value [*Kirk et al.*, 1995].

Elongation, E, quantifies the length to width relationship, $E = (l - w) / l$, having values ranging from 0, for perfect circles and squares, to 1, for elongate particles. Elongation is an indication of overall form and, unlike circularity, is not affected by surface roughness (Figure 8). Particle width and length are measured using the major and minor axes of a best-fit ellipse with the same area as the analyzed particle. Scatter plots of circularity, solidity, and elongation versus particle diameter, and histograms showing the distribution of these shape data are used to compare shape characteristics as a function of mineralogy and increasing shear strain.

5. RESULTS

5.1. Relative Abundance of Mineral Phases

The mineral phase maps are used to determine the relative abundance of quartz, orthoclase, oligoclase, and laumontite in each structural unit (Table 1). These phases constitute 92 to 98% of the total area of each image. Minor phases, including illite, epidote, apatite, and Fe-oxide, account for the remaining area. We report the relative abundance of the major phases in the following section. The values given for quartz, plagioclase, and orthoclase are for individual identifiable grains. The values given for laumontite includes fracture-fill that often is highly fractured, new grains of laumontite, cataclasized particles of laumontite, altered regions, and vein-fill.

In the BSS unit, ~77% of the area is taken up by clasts and ~23% of the area by laumontite. Plagioclase (oligoclase and albite) constitutes ~35% of the total clast area, ~35% is orthoclase, and ~30% is quartz. For the MB unit, clasts make up ~71% of the total area and the remaining ~29% is laumontite. Relative to the total clast area, ~38% is plagioclase, ~31% is orthoclase, and ~31% is quartz. Approximately 34% of the MBS area is occupied by clasts while ~66% of the area is laumontite. Plagioclase accounts for ~44% of the total clast area, orthoclase occupies ~24%, and quartz occupies ~32% of the clast area.

Plagioclase is the most abundant clast phase, displaying a substantial decrease in relative abundance from the BSS to the MBS. Quartz and orthoclase particles have similar total abundances that do not change with increasing shear, except for a small

decrease in orthoclase in the MBS, relative to the MB and BSS. Clasts dominate the total area in the BSS and MB, even though the area of clasts decreases slightly from the BSS to the MBS. The MBS displays a shift from a clast-dominated to a matrix-dominated unit.

5.2. Particle Size Distributions

The PSDs of quartz, orthoclase and plagioclase are determined for each magnification, normalized by the imaged area, and then plotted to illustrate the composite PSD for each mineral (Figure 9). The D and fractal limits for each mineral phase in each structural unit are reported in Table 2. All particle size distribution curves show a significant change in slope at each end (Figure 7). These changes in slope may represent a shift in the active mechanism of comminution, or most likely, reflect sampling effects [e.g., Bonnet et al., 2001], the implications of which are discussed later. In the BSS unit, the particle size range best fit by a power law distribution is approximately 6 to 200 μm for plagioclase, 5 to 252 μm for quartz, and 8 to 200 μm for orthoclase. The best-fit D for plagioclase and quartz is ~1.1 and is ~1.3 for orthoclase. When all mineral phases are combined, D is ~1.1 (Table 2).

In the MB structural unit, the particle size range best fit by a power-law distribution is approximately 1 to 316 μm for plagioclase, 0.5 to 398 μm for quartz, and 2 to 381 μm for orthoclase. The best-fit Ds for the different areas evaluated range from ~1.5 to 2.0 for plagioclase, ~1.0 to 1.4 for quartz, and ~1.6 to 2.0 for orthoclase. When all phases are combined, the D ranges from ~1.3 to 1.7 (Table 2); this is greater than the

D for the combined phases in the BSS, and reflects an overall increase in the relative number of small particles in all phases.

In the MBS structural unit, the particle size range best fit by a power-law distribution is approximately 0.3 to 89 μm for plagioclase, 1.5 to 125 μm for quartz, and 1 to 80 μm for orthoclase. The best-fit Ds for the different areas evaluated range from ~1.8 to 2.5 for plagioclase, ~1.5 to 2 for quartz, and ~1.5 to 2.5 for orthoclase. When all phases are combined, the D ranges from ~1.7 to 2.1 (Table 2); this is greater than the D for the combined phases in the BSS (Table 2), and reflects an overall increase in the relative number of small particles in all phases. The Ds for quartz are less than those for plagioclase and orthoclase, but similar to the range of Ds determined for the combined phases. Overall, the Ds for all phases in the MBS are greater than corresponding values in the MB and BSS (Table 2).

5.3. Particle Shape

Circularity, solidity, and elongation are shown for each mineral as a function of grain size and shear strain, by combining all of the shape data for each structural unit from the three faults studied (Figure 10). The variation in shape with grain size is shown with scatter plots of size versus shape descriptor, and with frequency distribution plots for two size bins, 5 to 25 μm (small grain-size fraction) and > 25 μm (large grain-size fraction). The statistical descriptors of the frequency distributions for circularity, solidity, and elongation are summarized in Tables 3, 4, and 5, respectively.

The distributions of particle circularity are fairly symmetric for all phases, grain sizes, and degrees of shear strain (Figure 10a). The frequency distributions for orthoclase are slightly more symmetric compared to plagioclase and quartz, and show a general broadening of the distribution with shear. The mean, skewness and kurtosis of the circularity distributions for all mineral phases show very little change for the fine-grain fraction with an increase in strain (Table 3). For the coarse-grain fraction, the mean and skewness of circularity decrease with strain in quartz and orthoclase, but not in plagioclase. In general, the large grain-size fraction produces lower mean circularity values when compared to the smaller particle sizes.

The distributions of particle solidity are distinctly asymmetric for all phases, grain sizes, and degrees of shear strain (Figure 10b). The distribution is narrower for coarse particles and broadens with a decrease in grain size. The mean, skewness and kurtosis of the solidity distributions show little change with shear in the fine-grain fraction, but show a slight decrease in the mean and skewness of solidity, particularly for quartz, in the coarse-grain fraction (Table 4). Overall, the mean solidity values are higher for the large grain-size fraction relative to the small grain-size fraction.

In general, the distributions of particle elongation are symmetric for all phases, grain sizes, and degrees of shear strain (Figure 10c). Minor asymmetry towards lower elongation values, however, is observed for quartz and plagioclase in both the BSS and MBS structural units, reflecting slightly more rounded particles. For all mineral phases in the fine grain-size fraction, there is a slight decrease in the mean elongation, and a decrease in the skewness of the distribution for plagioclase and quartz with shear (Table

5). The mean of elongation for the coarse-grain fractions of plagioclase and orthoclase decreases slightly with shear, but does not show consistent changes for quartz. Overall, the large particle size fraction has lower mean elongation values compared to the fine particle size fraction.

For circularity, solidity, and elongation, two grain-size clusters are observed in the BSS (most prevalent for orthoclase), and become slightly less obvious in the MB. The large grain-size cluster of particles is not observed in the MBS (Figure 10). The skewness of the elongation distributions decreases from the BSS to the MB, and then increases again for the MBS. This is the case for almost all phases and grain sizes, with the exception of a small fraction of quartz.

5.3.1. Relationships between shape characteristics

The shape descriptors are not completely independent characteristics. Accordingly, the shape descriptors are further investigated through cross plots of circularity versus solidity for binned values of elongation (Figure 11 and 12). Elongation is grouped into four bins, each with an equal number of particles (Figure 12). In all cases, circularity and solidity are positively related, and both show a negative relationship to elongation. In general, grains with low elongation also have high solidity and circularity, and those with high elongation are defined by low solidity and circularity.

Although all cases show similar trends in circularity, solidity, and elongation, there are distinct differences in when mineralogy, shear strain, and grain size are considered. Quartz and plagioclase have similar circularity-solidity-elongation

relationships in both the BSS and MBS (Figure 12), though quartz tends to have a greater percentage of particles with very high circularity and solidity, and low elongation, i.e., particles that are smoother and more circular. For these two minerals, the solidity values of particles from the most highly sheared regions (MBS) are about 0.04 less than those for the least sheared region (BSS) (Figure 12).

Orthoclase shows similar circularity-solidity-elongation trends as quartz and plagioclase, but the solidity values are less than those for quartz and plagioclase by about 0.04 for corresponding shear strains. In addition, the orthoclase particles display significantly lower circularity and solidity when compared to quartz and plagioclase from the same elongation bin.

The difference in solidity values between the highly sheared regions and the least sheared regions, in part, reflects the fact that there are a relatively large number of large particles in the BSS, and that the large particles have high values of solidity (Figure 11a). The solidity values of the fine-grained fraction of the BSS (Figure 11a) are similar to those in the more highly sheared material (Figure 11b), although the comparison is difficult to make definitively because of the small number of fine particles in the BSS.

6. DISCUSSION

6.1. Fractal Size Distributions and Fractal Limits

The particle size distributions analyzed for each of the three size-classes of subsidiary faults can be described by a power-law relationship for sizes ranging over 3 orders of magnitude (Table 2). In this study, we define the limits of the power-law relationship by the distinct slope changes at the upper and lower extremes of particle sizes measured (Figure 7). Although these limits are used to fit the power-law are referred to as fractal limits, this does not necessarily mean that the fractal scaling relations do not extend to larger and smaller particle sizes. Herein, the limits largely reflect sampling errors and resolution limits.

The lower fractal limit of the PSD at particle sizes of approximately 0.3 μm in diameter, predominately is caused by the limited resolution of the mineral phase maps constructed by element mapping. The high-resolution X-ray maps were acquired at a quarter-micron per pixel resolution. Isolated single or pairs of pixels, however, are not used for phase identification because of likely X-ray contamination from underlying phases that can occur when the X-ray excitation volume is greater than that of the smallest particle size [*Gottlieb et al.*, 2000]. Careful examination of high magnification (2400X and 9600X) BSE images, taken in the highly sheared regions, provides proof for the existence of submicron particles that are smaller than those resolved by mineral phase mapping, and therefore were not included in the phase-specific particle size measurements.

The bias caused by the limited resolution of the phase maps can only explain a change in slope for the small particles. The following two sampling effects, however, can explain the deviation in slope for both ends of the PSD curve. First, regions for analysis should be chosen at random, but because of the limited sample area with increasing magnification, regions were chosen preferentially to avoid large particles that would dominate the field of view, which causes a bias in the distribution of large particles [*Sammis et al.,* 1987; *Bonnet et al.* 2001]. Second, there may be a misrepresentation of small particles that are either overlooked or not intersected by the thin section [*Blenkinsop*, 1991]. This bias could work in conjunction with the limited resolution of the phase map to generate unreliable PSD data for the finest particles sizes.

The sampling errors and the limitations imposed by phase resolution, do not affect the PSDs in the size ranges sampled within the range of overlapping magnifications, which correspond to the portion of the PSD that is demonstrably fractal. Thus, the values of D determined are robust and may be used to characterize and compare the PSD of the different mineral phases and different structural units, as well as with the PSDs determined in other studies. The entire range of D (1-2.5) determined in the present study falls within the range of fractal values (0.8-2.6) observed in naturally deformed rocks [e.g. *Sammis et al.*, 1987; *Blenkinsop*, 1991; *Storti et al.*, 2003; *Chester et al.*, 2005; *Keulen et al.*, 2007; *Bjørk et al.*, 2009], and 72% of the values of D determined are between ~ 1.5 and 2.1, which are the most common values of Ds documented in natural fault rocks and produced in experimental shear zones [e.g.

Sammis et al., 1987; *Biegel et al.*, 1989; *Marone and Scholz*, 1989; *Sammis and King*, 2007].

6.2. Comminution Processes

Sammis et al. [1987] proposed a constrained comminution model to explain the fractal geometry observed for low strain gouge and breccia. They reasoned that the relatively high confining pressure associated with fault formation prevents grains from moving freely relative to one another (i.e., grains are constrained), increasing the probability that fracture of a particle is controlled by the relative size of neighboring particles. For compressive shear of granular material, stress is concentrated and largely carried by grain bridges. The conditions that favor bridge failure form locally at the contact between two similar-sized particles. During shear the bridges undergo rotation and a reduction in normal stress perpendicular to the loaded grain contacts leading to a grain-scale uniaxial compressive stress state, and ultimately, tensile failure of one of the grains. The end result of repeated bridge formation and fracture is a self-similar gouge composed of particles with dissimilar-sized neighbors and a PSD with a $D \sim 1.6$. In contrast, unconstrained comminution occurs when particles can move freely relative to one another, promoting the processes of pounding (i.e., impact) and milling (i.e., grinding and abrasive wear). For many models of unconstrained comminution, the probability of fracture is determined by the presence of starter flaws and pre-existing weaknesses [*Sammis and King*, 2007; *Sammis and Ben-Zion*, 2008]. To a large extent,

the PSD observed here are consistent with comminution under constrained conditions, at least at the lower shear strains.

The PSDs within the BSS unit (Figure 9) are characterized by a low D (~1.1-1.3) for particles between the lower limits of 5 to 8 μm and upper limits of 200 to 250 μm (Table 2). Particle sizes of ~ 3μm in diameter were successfully analyzed but these clearly are fewer in number and below the fractal limit. *Mair et al.* [2002] and *Billi* [2007] suggest that for PSDs with low D, that small particles volumetrically are rare because the fault rocks likely have undergone less comminution overall. Microstructures in the less deformed structural units, described herein, are similar to the structures described by these workers. The FSS and BSS show similar sized particles in contact in addition to many examples of tensile fractures splitting grains. An additional feature of the FSS and BSS units is the presence of laumontite cement that surrounds the larger particles and limits contact between the smaller clastic particles. The lack of small particles in conjunction with the presence of same-size neighbors implies that these zones represent early stages of deformation where the magnitude of shear and extent of fracture are insufficient to match the assumptions of the constrained comminution model or to evolve to a fractal geometry where D ~ 1.6.

The PSD within the MB unit (Figure 9) yields an average D of ~1.8, ~1.7, and ~1.3 for orthoclase, plagioclase, and quartz, respectively. These values are greater than those measured for the BSS, consistent with the qualitative observation that the MB units have a greater number of small particles that extend down to at least 0.5 μm in diameter (Table 2). Although the D measured for the different phases in the MB unit

does not equal the value of 1.6 predicted by *Sammis et al.* [1987] for particle size reduction by constrained comminution, the average value for all phases combined is very close to 1.6. Particles with same-size and same phase neighbors are rare in the MB unit, and tensile fractures splitting large grains are common, becoming progressively less frequent in the smaller grains (Figure 6b). These observations are consistent with repeated bridge-formation, tensile fracturing of grains, and sufficient shear strain to produce the PSD characteristic of constrained comminution

The PSD recorded for the MBS unit (Figure 9) displays fractal geometries for particles between the lower limits of 0.03 to 9 μm and upper limits of 22 to 125 μm. These distributions are best-fit by a higher D of ~2, ~2, and ~1.8 for orthoclase, plagioclase, and quartz, respectively. The full range of Ds recorded for the mineral phases in the MBS is much broader, however, extending from ~1.5 to 2.5 (Table 2). The greatest values of D measured are for plagioclase and orthoclase in the MBS of the large subsidiary fault in Zones 2 and 3, which are highly sheared and contain large amounts of laumontite. Observed values of $D \geq 2$ are consistent with previously recorded values for intensive shear localization in cataclastic rocks [*Blenkinsop*, 1991; *An and Sammis*, 1994; *Blenkinsop and Fernandes*, 2000; *Storti et al.*, 2003; *Heilbronner and Keulen*, 2006; *Keulen et al.*, 2007; *Bjørk et al.*, 2009], as well as in experimental shear zones with localization of strain [e.g., *Biegel et al.*, 1989; *Marone and Scholz*, 1989]. Comminution during shear of Westerly Granite [*Biegel et al.*, 1989] and quartz [*Marone and Scholz*, 1989] gouges, produced PSDs defined by a D consistent with constrained comminution except in localized shear bands (e.g., Riedel shears), where particle sizes

are smaller overall, and D is greater, typically around 2. Both natural and experimental high-strain, localized shear zones likely have undergone particle size reduction by either selective fracture of large particles [*Sammis and King*, 2007], or shear-enhanced inter-particle slip with associated abrasion and wear of the large particles contained within a fine-grain matrix [e.g. *An and Sammis*, 1994; *Billi*, 2005; *Keulen et al.*, 2007; *Storti et al.*, 2003; *Blenkinsop*, 1991].

The overall progressive increase in D from ~1.6 to ~ 2.0 with increasing shear strain, seen in this (Figures 13 and 14) and previous studies, has been addressed [*Sammis and King*, 2007] by extending the constrained comminution model to include processes at larger shear strains. Specifically, under constrained comminution, the occurrence of similar-sized, nearest-neighbor particles is greatly reduced; however, with increasing shear and flow of particles, the constraint on particle motion is relaxed and same-sized particles are brought into contact. Particle fracture then depends on the probability of similar-sized particles coming into contact. *Sammis and King* [2007] conclude that for a D less than 2.0, the probability of contact between same-sized neighbors is greater for larger particles, and as a result, larger particles are preferentially fractured leading to an increase in D with strain.

An important result from our analysis of the PSD of a polyphase material is that the value of D often varies with phase. At all shear strains and in all structural units, the D of quartz is less than that of orthoclase and plagioclase (Figure 14). We hypothesize that this relation reflects a difference in the material properties of the phases, specifically the greater fracture strength of quartz at these conditions and the propensity for cleaving

in the feldspars. *Bjork et al.* [2009] document a relationship between mineralogy and the PSD of granodiorite fault rocks, where the D of orthoclase is greater than that of plagioclase and quartz combined. This is consistent with our observations; however by analyzing quartz and plagioclase independently we demonstrate that the PSD of quartz has a lower D when compared to plagioclase (Figure 14). In earlier studies, *Evans* [1988] observed that the average size of feldspar particles is less than that for quartz particles in naturally faulted granitic gneisses, and related the size difference to the comparatively weaker strength of feldspar, as well as the possibility for cracks in quartz to heal at shallow crustal conditions [*Evans*,1988 and *Blenkinsop and Sibson*, 1992].

The effect of different material properties in a polyphase aggregate can be understood in the context of the constrained comminution model [*Sammis et al.*, 1987] and other nearest-neighbor models [*Sammis and King*, 2007]. Assume an aggregate that consists of two phases, equal in volume, but different in fracture strength. In this case, fracture of a particle of the weaker phase is favored for contacting particles of similar size if either one or both of the particles is the weaker phase. Fracture of the stronger phase is favored only for the case of two similar-sized, contacting particles of the stronger phase. Given the greater frequency for formation of contacting pairs composed of at least one particle of the weaker phase, the rate of comminution in the weaker phase should exceed that of the stronger phase, resulting in a greater D for the weaker phase. In the case of the subsidiary faults in the arkosic sandstones from SAFOD, where the volume fraction of feldspar is twice that of quartz, and quartz has greater fracture

strength at 3 km depth, the D of the PSDs for quartz should be lower than that of the feldspars in all structural units, as observed in this study.

6.3. Insights into Fragmentation Processes from Shape Characteristics

The PSD data for the clasts in the arkosic sandstone suggest that the FSS and BSS units represent early stages of deformation where the magnitude of shear strain and extent of fracture are insufficient to match the assumptions of the constrained comminution model. However, the constrained comminution model provides a good description for deformation in the MB unit of the subsidiary faults at SAFOD. When shear strains are high and the D of particles within the fault are greater than the predicted value of 1.6, the constrained comminution model no longer explains all of the observations. At this point, fracture preferentially occurs in the larger particles as suggested by Sammis and King [2007].

Data from this study demonstrates that there is a significant mineral phase effect. Specifically, quartz tends to break down at a slower rate, relative to the feldspar phases, as the deformation processes begin to shift from constrained comminution to more distributed shearing and granular flow [e.g., *Marone and Scholz*, 1989; *Sammis and King*, 2007]. This progressive shift in processes enhances surface wear; abrasion and chipping increase in importance as grain-splitting and fragmentation continue [e.g. *Storti et al.*, 2003; *Billi*, 2005; *Keulen et al*., 2007]. Because the comminution rate of quartz is slower than that in feldspar, quartz experiences a greater degree of surface wear between grain-splitting events that leads to greater rounding of the grains.

The shape data are consistent with the hypotheses derived from the PSD data. In the BSS, the large particles have high circularity and solidity, reflecting shapes that are generated during sedimentary processes, i.e., shapes that reflect the breakdown of a crystalline rock and separation of grains along phase boundaries during sediment transport. Comminution during faulting produces a decrease in solidity and a broadening of the elongation distribution. Changes in circularity are much more subtle, likely reflecting the fact that circularity depends on surface roughness and overall form [*Crompton*, 2005]. These observations are consistent with the breakdown of particles by tensile fracture and fragmentation, processes expected at low shear strains.

In the MB and MBS, in contrast, the entire particle population experiences a shift to lower solidity values and a broader elongation distribution, reflecting the fact that all particles by this point have experienced fragmentation to some degree because of the higher shear strain. It is notable that orthoclase displays significantly lower solidity in the MBS, relative to quartz, consistent with the influence of cleavage that favors particle breakdown, and leads to a higher rate of comminution.

The shape characteristics for plagioclase are more like those of quartz, even though plagioclase also has well-defined cleavage similar to orthoclase. This can be explained by the fact that although plagioclase does fracture along cleavages, it has a much higher propensity for alteration that would tend to occur at a greater rate along rougher surfaces, and thus promote more rapid smoothing following cleaving events.

The MBS is the most highly sheared unit investigated in this study. Particles within this unit should display the greatest degree of abrasion, chipping, and rounding of

particles. In addition, because of its relative resistance to fracture and greater residence times between splitting events, quartz, in particular, should demonstrate a mineral phase affect, if one exists. This hypothesis is supported by a comparison of the shape characteristics of quartz to orthoclase (Figure 12). A much larger fraction of quartz particles have high circularity, solidity, and elongation when compared to orthoclase.

6.4 Origin and Influence of Laumontite

Feldspars present in the subsidiary fault samples have undergone both physical and chemical alteration. Host oligoclase has undergone albitization, where the anorthite component is replaced by albite causing the release of Ca^{2+}, Al^{3+}, and OH^{-} into the system. These ions with the addition of silica form a hydrated zeolite called laumontite [*Blenkinsop and Sibson*, 1992; *Evans and Chester*, 1995]. Laumontite may also form by the direct alteration of oligoclase to laumontite. Blenkinsop and Sibson [1992] observe dilatant textures in plagioclase grains that are caused by the 60% molar volume increase that occur as a result of the direct alteration of plagioclase to laumontite. Although there likely is some in situ laumontization, most of the laumontite associated with the shear zones appears to be produced by albitization. Abundant laumontite cement seals many inter- and intragranular fractures and largely makes up the matrix for each structural unit (Figure 6a, b, and c). The observed large quantity of laumontite raises the possibility that some laumontite has been introduced by advection. Large fracture pathways in the SAF damage zone could provide the opportunity for fluid advection from more distant sources, both laterally and from depth [Chester, pers. comm., 2011]. However, a

systematic study over the entire 12 m of sedimentary core would be required to provide more evidence about the origin of laumontite in this system.

Understanding the effect of laumontite on particle size reduction processes and the resultant Ds is crucial because of the large quantity of laumontite in this system. Morrow and Byerlee [1991] use samples from surface outcrops near the locality of the Cajon Pass drillhole to study the frictional properties of laumontite. Many of the fault zones intersected by the drillhole contain laumontite that appears to be acting as fault gouge. The goal of their study is to determine if this fault zone laumontite is causing a reduction in the shear strength of these faults, similar to the low-shear strength of clay-rich fault gouges. Friction studies on the laumontite fault gouge show behavior similar to other strong crustal rocks and no effective decrease in shear strength of the fault zone. If laumontite in FSS, BSS, MB and MBS units of the subsidiary faults at SAFOD has the same mechanical properties described by Morrow and Byerlee [1991], then it is expected that laumontite would aid in the comminution of the entrained clasts and display textural evidence for brittle deformation features. However, if the laumontite gouge is mechanically weak, it is anticipated that laumontite would act as a buffer to comminution resulting in smaller amounts of particle size reduction of the enclosed clasts. Figure 15 plots percent laumontite as a function of D for each sample region. The trend displays a general increase in the percent laumontite with an increase in D. However, a few data points (circled in Figure 15) do not appear to be consistent with this observation. All four values were measured in the MBS unit for regions characterized as sheared dilatant veins. One possible explanation for these outlier Ds, is that the timing of

vein formation influences the Ds measured within sheared dilatant veins. The observed increase in D with an increase in laumontite abundance, along with microstructural evidence from BSE images showing fractured blocks of laumontite (Figure 16), implies laumontite is mechanically strong and is likely aiding in the comminution of clasts in the arkosic sandstone.

7. CONCLUSIONS

We use X-ray maps and BSE images to quantify the evolution of particle size and shape, as a function of mineralogy and shear strain, in faulted arkosic sandstone samples collected at 3 km depth from the western damage zone of the SAF, approximately 130 m west of the SDZ at SAFOD. These data are used to constrain the processes of grain size reduction and healing of subsidiary faults cutting the damage zone to better understand the evolution of off-fault damage and strength recovery. Subsidiary faults from different size-classes and specific structural units within these faults provide samples representing different magnitudes shear strain and fault zone healing. Particle mineralogy is determined from detailed element maps, while BSE images provide a definition of grain boundaries and microfracture geometries. Particle shape is characterized in terms of circularity, solidity, and elongation.

1. The distribution of particle sizes in each structural unit is best described as fractal over the particle size range investigated (0.3 μm < d < 400 μm), particularly in the more highly sheared units. The fractal dimension, D, of the PSD increases with increasing shear strain, where the smallest average D (~1.1-1.3) is found in the brecciated sandstone, an intermediate D (~1-2) defines the microbreccia, and the greatest D (~1.5-2.5) defines the microbreccia with shears for quartz, orthoclase, and plagioclase.
2. For the quartz, magnitude of D is slightly smaller than that for plagioclase and orthoclase reflecting the greater fracture toughness of quartz relative to fracture along

cleavage in the feldspars.

3. The lower fractal limit of the PSDs likely reflects truncation due to limits in resolving the mineralogy of particles less than 0.3 μm in diameter. So the expected change in fractal dimension associated with the grinding limit is not explored in this study.
4. The relations between particle shape characteristics vary with shear strain and grain size. Overall, fracture and cleavage at low strains lead to a reduction in solidity and an increase in circularity and elongation from the undeformed sedimentary rocks. With increasing shear strain and particle size reduction elongation is reduced, and circularity and solidity are slightly increased.
5. The volume fraction of laumontite, which reflects the alteration of oligoclase to albite and laumontite, increases with increasing shear strain, and thus with an increase in D. The increase in percent laumontite with D reflects repeated episodes of fracture and cementation in the subsidiary faults as shape and size of particles evolve.
6. The overall increase in D and evolution of shape with increasing shear strain reflects a progressive change in the relative contribution of comminution mechanisms from grain-splitting and crushing (constrained comminution), that dominates at low shear strains, to surface abrasion and chipping, that dominate at high shear strains.

REFERENCES

Almeida, R. (2007), Mesoscale fracture fabric and paleostress along the San Andreas Fault at SAFOD, M.S. thesis, Dep. of Geol. and Geophys., Texas A&M University, College Station, TX.

An, L.-J., and C. G. Sammis (1994), Particle size distribution of cataclastic fault materials from Southern California: A 3-D study, *Pure Appl. Geophys.*, *143*(1), 203-227, doi:10.1007/bf00874329.

Andrews, D. J. (2005), Rupture dynamics with energy loss outside the slip zone, *Geophys. Res.*, *110*, B01307, 1-14, doi:10.1029/2004jb003191.

Biegel, R. L., and C. G. Sammis (2004), Relating fault mechanics to fault zone structure, *Adv. in Geophys.*, *47*, 66-113.

Biegel, R. L., C. G. Sammis, and J. H. Dieterich (1989), The frictional properties of a simulated gouge having a fractal particle distribution, J. *Struct. Geol.*, *11*(7), 827-846, doi:10.1016/0191-8141(89)90101-6.

Billi, A. (2004), Fractal distribution of particle size in carbonate cataclastic rocks from the core of a regional strike-slip fault zone, *Tectonophys.*, *384*(1-4), 115-128, doi:10.1016/j.tecto.2004.03.015.

Billi, A. (2005), Grain size distribution and thickness of breccia and gouge zones from thin (<1m) strike-slip fault cores in limestone, *J. Struct. Geol.*, *27*(10), 1823-1837, doi:10.1016/j.jsg.2005.05.013.

Billi, A. (2007), On the extent of size range and power law scaling for particles of natural carbonate fault cores, *J. Struct. Geol., 29*(9), 1512-1521, doi:10.1016/j.jsg.2007.06.007.

Bjørk, T. E., K. Mair, and H. Austrheim (2009), Quantifying granular material and deformation: Advantages of combining grain size, shape, and mineral phase recognition analysis, *J. Struct. Geol.*, *31*(7), 637-653, doi:10.1016/j.jsg.2009.03.020.

Blenkinsop, T. G. (1991), Cataclasis and processes of particle size reduction, *Pure Appl. Geophys., 136*(1), 59-86.

Blenkinsop, T. G., and R. H. Sibson (1992), Aseismic fracturing and cataclasis involving reaction softening within core material from the cajon pass drill hole, *J. Geophys. Res., 97*(B4), 5135-5144.

Blenkinsop, T. G., and T. R. C. Fernandes (2000), Fractal characterization of particle size distributions in chromitites from the Great Dyke, Zimbabwe, *Pure Appl. Geophys., 157*, 505-521.

Blythe, A. E., M. A. d'Alessio, and R. Burgmann (2004), Constraining the exhumation and burial history of the SAFOD pilot hole with apatite fission track and (U-Th)/He thermochronometry, *Geophys. Res. Lett.,31*(15), doi:10.1029/2003gl019407.

Boles, J. R. (1982), Active albtization of plagioclase, Gulf Coast Tertiary, *Am. J. Sci.*, *282*, 165-180.

Boles, J. R., and D. S. Coombs (1977), Zeolite facies alteration of sandstones in the Southland Syncline, New Zealand, *Am. J. Sci.*, *277*(8), 982-1012, doi:10.2475/ajs.277.8.982.

Bonnet, E., O. Bour, N. E. Odling, P. Davy, I. Main, P. Cowie, and B. Berkowitz (2001), Scaling of fracture systems in geologic media, *Rev. Geophys.*, *39*(3), 347-383.

Bradbury, K. K., D. C. Barton, J. G. Solum, S. D. Draper, and J. P. Evans (2007), Mineralogic and textural analyses of drill cuttings from the San Andreas Fault Observatory at Depth (SAFOD) boreholes: Initial interpretations of fault zone composition and constraints on geologic models, *Geosphere*, *3*(5), 299, doi:10.1130/ges00076.1.

Catchings, R. D., M. J. Rymer, M. R. Goldman, J. A. Hole, R. Huggins, and C. Lippus (2002), High-resolution seismic velocities and shallow structure of the San Andreas Fault Zone at Middle Mountain, Parkfield, California, *Bull. Seismol. Soc. Am.*, *92*(6), 2493-2503, doi:10.1785/0120010263.

Chester, F. M., J. P. Evans, and R. L. Biegel (1993), Internal structure and weakening mechanisms of the San Andreas Fault, *J. Geophys. Res., 98*(B1), 771-786.

Chester, F. M., J. S. Chester, D. L. Kirschner, S. E. Schulz, and J. P. Evans (2004), Structure of large-displacement, strike-slip fault zones in the brittle continental crust, *Rheology and Deformation in the Lithosphere at Continental Margins*, Edited by Karner, G. D., B. Taylor, N. W. Driscoll, and D. L. Kohlstedt, pp. 1-42, Columbia University Press, New York.

Chester, J.S. (2011), Personal Communication.

Chester, J. S., F. M. Chester, and A. K. Kronenberg (2005), Fracture surface energy of the Punchbowl fault, San Andreas system, *Nature*, *437*(7055), 133-136, doi:10.1038/nature03942.

Chester, J. S., F. M. Chester, D. Kirschner, R. Almeida, J. P. Evans, G. R.N., S. Hickman, M. Zoback, and W. Ellsworth (2007), Deformation of sedimentary rock across the San Andreas Fault Zone: Mesoscale and microscale structures displayed in core from SAFOD, *Eos Trans. AGU*, *88(52)*, Fall Meet. Suppl., Abstract T42C-05.

Chester, J. S., F. M. Chester, D. Kirschner, J. P. Evans, D. W. Sills, and C. G. Coble (2008), Structure of the San Andreas Fault Zone at SAFOD, paper presented at Geological Society of America Annual Meeting, Houston, TX. Abstract.

Clarke, S.H., and T.H. Nilsen (1973), Displacement of Eocene strata and implication for the history of offset of the San Andreas fault, central and northern California, in *Proceedings of the Conference on Tectonic Problems of the San Andreas Fault System,* edited by R.L. Kovach, and A. Nur, pp. 358–367, Stanford University Publications in Geological Sciences, Palo Alto, Calif.

Cromtpon, C. (2005), Particle shape: An important parameter in pharmaceutical manufacturing, *Pharmaceutical Manufacturing and Packing Sourcer*, http:// www.samedanltd.com/magazine/15/issue/55.

Dickinson, W. R. (1966), Structural Relationships of San Andreas Fault System, Cholame Valley and Castle Mountain Range, California, *Geol. Soc. Am. Bull., 77*(7), 707-726, doi:10.1130/0016-7606(1966)77[707:srosaf]2.0.co;2.

Draper-Springer, S., J. P. Evans, J. I. Garver, D. Kirschner, and S. U. Janecke (2009), Arkosic rocks from the San Andreas Fault Observatory at Depth (SAFOD) borehole, central California: Implications for the structure and tectonics of the San Andreas Fault Zone, *Lithosphere*, *1*(4), 206-226, doi:10.1130/l13.1.

Engelder, J. T. (1974), Cataclasis and the generation of fault gouge, *Geol. Soc. Am. Bull., 85*(10), 1515, doi:10.1130/0016-7606.

Evans, J. P. (1988), Deformation mechanisms in granitic rocks at shallow crustal levels, *J. Struct. Geol., 10*(5), 437 - 443.

Evans, J. P., and F. M. Chester (1995), Fluid-rock interaction in faults of the San Andreas system: Inferencesf rom San Gabriel fault rock geochemistry and microstructures, *J. Geophys. Res., 100*(B7), 13,007-013,020.

Exner, H. E. (1972), Analysis of grain- and particle-size distributions in metallic materials, *Int. Met. Rev.,159*, 29-42.

Falconer, K. J. (1985), *The Geometry of Fractal Sets*, Cambridge University Press, Cambridge, England.

Faulkner, D. R., T. M. Mitchell, E. Jensen, and J. Cembrano (2011), Scaling of fault damage zones with displacement and the implications for fault growth processes, *J. Geophys. Res., 116*(B5), doi:10.1029/2010jb007788.

Gottlieb, P., G. Wilkie, D. Sutherland, E. Ho-Tun, S. Suthers, K. Perera, B. Jenkins, S. Spencer, A. Butcher, and J. Rayner (2000), Using quantitative electron microscopy for process mineralogy applications, *JOM*, *52*(4), 24-25.

Graham, S. A. (1978), Role of sallnian block in evolution of San Andreas Fault system, Callfornia, *AAPG Bull.,62*(11), 2214-2231.

Heilbronner, R., and N. Keulen (2006), Grain size and grain shape analysis of fault rocks, *Tectonophys.*, *427*(1-4), 199-216, doi:10.1016/j.tecto.2006.05.020.

Heron, B., J. S. Chester, R. Guillemette, and F. M. Chester (2011), Comminution and mineralization of subsidiary faults in the damage zone of the San Andreas Fault at SAFOD, poster presented at Earthscope National Meeting, Austin, TX, Abstract.

Imber, J., R. E. Holdsworth, S. A. F. Smith, S. P. Jefferies, and C. Collettini (2008), Frictional-viscous flow, seismicity and the geology of weak faults: a review and future directions, *Geol. Soc. Lond., Spec. Pub.*, *299*, 151-173.

Kanamori, H. (1994), Mechanics of earthquakes, *Annu. Rev. Earth Planet. Sci.*, *22*, 207-237.

Kanamori, H. (2004), The diversity of the physics of earthquakes, *Proc. Japan Acad., Series B*, *80*, 297-316.

Keulen, N., R. Heilbronner, H. Stunitz, A. Boullier, and H. Ito (2007), Grain size distributions of fault rocks: A comparison between experimentally and naturally deformed granitoids, *J. Struct. Geol., 29*(8), 1282-1300, doi:10.1016/j.jsg.2007.04.003.

Kirk, T. B., D. Panzera, R. V. Anamalay, and Z. L. Xu (1995), Computer image analysis of wear debris for machine condition monitoring and fault diagnosis, *Wear*, *181-183*, 717-722.

Kistler, R. W., and D. E. Champion (1986), Rb-Sr whole-rock and mineral ages, K-Ar, 40Ar/39Ar, and U-Pb mineral ages, and strontium, lead, neodymium, and oxygen isotopic compositions for granitic rocks from the Salinian Composite Terrane, California, *U.S. Geological Survery Open-File Report*, *01-453*, 1-80.

Krumbein, W. C., and F. C. Pettijohn (1990), *Manual of Sedimentary Petrography*, Soc. Sed. Geol., SEPM Reprint Ser. 13, 1-549.

Ma, S., and R. J. Archuleta (2006), Radiated seismic energy based on dynamic rupture models of faulting, *J. Geophys. Res., 111*(B05315), doi:10.1029/2005JB004055.

Mair, K., K. M. Frye, and C. Marone (2002), Influence of grain characteristics on the friction of granular shear zones, *J. Geophys. Res.*, *107*(B10), doi:10.1029/2001jb000516.

Mandelbrot, B. B. (1982), *Fractals and the Geometry of Nature*, Freeman and Co, New York.

Marone, C., and C. H. Scholz (1989), Particle-size distribution and microstructures within simulated fault gouge, *J. Struct. Geol., 11*(7), 799-814.

McPhee, D. K., R. C. Jachens, and C. M. Wentworth (2004), Crustal structure across the San Andreas Fault at the SAFOD site from potential field and geologic studies, *Geophys. Res. Lett.,31*(12), doi:10.1029/2003gl019363.

Morrow, C. A., and J. D. Byerlee (1991), A note on the frictional strength of laumontite from Cajon Pass, California, *Geophys. Res. Lett.,18*(2), 211-214.

Olgaard, D. L., and W. F. Brace (1983), The microstructure of gouge from a mining-induced seismic shear zone, *Int. J. Rock Mech. Min. Sci. & Geomech. Abstr.*, *20*(1), 11-19.

Page, B. M. (1981), The southern Coast Ranges, in *The Geotectonic Development of California*, edited by W. G. Ernst, pp. 329-417, Prentice-Hall, New York.

Rawling, G. C., and L. B. Goodwin (2003), Cataclasis and particulate flow in faulted, poorly lithified sediments, *J. Struct. Geol., 25*(3), 317-331, doi:10.1016/s0191-8141(02)00041-x.

Rockwell, T., M. Sisk, G. Girty, O. Dor, N. Wechsler, and Y. Ben-Zion (2009), Chemical and physical characteristics of pulverized Tejon Lookout granite adjacent to the San Andreas and Garlock Faults: Implications for earthquake physics, *Pure Appl. Geophys., 166*(10-11), 1725-1746, doi:10.1007/s00024-009-0514-1.

Rymer, M. J. C., R.D.; Godlman, M.R. (2003), Structure of the San Andreas Fault Zone as revealed by surface geologic mapping and high-resolution seismic profiling near Parkfield, California, paper presented at the *EGS - AGU - EUG Joint Assembly*, Nice France.

Sammis, C., G. King, and R. Biegel (1987), The kinematics of gouge deformation, *Pure Appl. Geophys., 125*(5), 777-812.

Sammis, C. G., and R. L. Biegel (1989), Fractals, fault-gouge, and friction, *Pure Appl. Geophys., 131*(1/2), 255-271.

Sammis, C. G., and G. C. P. King (2007), Mechanical origin of power law scaling in fault zone rock, *Geophys. Res. Lett.,34*(4), doi:10.1029/2006gl028548.

Sammis, C. G., and Y. Ben-Zion (2008), Mechanics of grain-size reduction in fault zones, *J. Geophys. Res., 113*(B2), doi:10.1029/2006jb004892.

Sammis, C. G., R. H. Osborne, J. L. Anderson, M. Banerdt, and P. White (1986), Self-similar cataclasis in the formation of fault gouge, *Pure Appl. Geophys., 124*(1/2), 53-78.

Savage, H. M., and E. E. Brodsky (2011), Collateral damage: Evolution with displacement of fracture distribution and secondary fault strands in fault damage zones, *J. Geophys. Res., 116*(B3), doi:10.1029/2010jb007665.

Scholz, C. H. (1987), Wear and gouge formation in brittle faulting, *Geology*, *15*(6), 493-495, doi:10.1130/0091-7613.

Scholz, C. H., N. H. Dawers, J.-Z. Yu, and M. H. Anders (1993), Fault growth and fault scaling laws: Preliminary results, *J. Geophys. Res., 98*(B12), 21,951-921,961.

Sibson, R. H. (1977), Fault rocks and fault mechanisms, *J. Geol. Soc. Lond.*, *133*, 191-213.

Sibson, R. H. (1986), Brecciation processes in fault zones: Inferences from earthquake rupturing, *Pure Appl. Geophys., 124*(1/2), 159-175.

Sibson, R. H. (2003), Thickness of the seismic slip zone, *Bull. Seismol. Soc. Am., 93*(3), 1169-1178.

Sills, D., 2010. The fabric of clasts, veins and foliations within the actively creeping zones of the San Andreas Fault at SAFOD: Implications for deformation processes, M.S.

thesis, Dep. of Geol. and Geophys., Texas A&M University, College Station, TX.

Solum, J. G., S. H. Hickman, D. A. Lockner, D. E. Moore, B. A. van der Pluijm, A. M. Schleicher, and J. P. Evans (2006), Mineralogical characterization of protolith and fault rocks from the SAFOD Main Hole, *Geophys. Res. Lett.,33*(21), doi:10.1029/2006gl027285.

Storti, F., A. Billi, and F. Salvini (2003), Particle size distributions in natural carbonate fault rocks: insights for non-self-similar cataclasis, *Earth Planet. Sci. Lett., 206*, 173-186.

Storti, F., F. Balsamo, and F. Salvini (2007), Particle shape evolution in natural carbonate granular wear material, *Terra Nova*, *19*(5), 344-352, doi:10.1111/j.1365-3121.2007.00758.x.

Templeton, E. L., and J. R. Rice (2008), Off-fault plasticity and earthquake rupture dynamics: 1. Dry materials or neglect of fluid pressure changes, *J. Geophys. Res., 113*(B9), doi:10.1029/2007jb005529.

Tinti, E., P. Spudich, and M. Cocco (2005), Earthquake fracture energy inferred from kinematic rupture models on extended faults, *J. Geophys. Res., 110*(B12), doi:10.1029/2005jb003644.

Turcotte, D. L. (1992), *Fractals and Chaos in Geology and Geophysics*, Cambridge University Press, New York.

Underwood, E. E. (1968), Particle-size distribution, in *Quantitative Microscopy*, edited by R. T. DeHoff and F. N. Rhines, pp. 151-201, McGraw-Hill, New York.

Watson, J. (1997), The San Andreas Fault – III. Where is it?, *USGS*, http://www.usgs.gov/.

Wibberley, C. A. J., and T. Shimamoto (2003), Internal structure and permeability of mahor strike-slip fault zones: the Median Tectonic Line in Mie prefecture, Southwest Japan, *J. Struct. Geol., 25*, 59-78.

Williams, M. L., K. E. Scheltema, and M. J. Jercinovic (2001), High-resolution compositional mapping of matrix phases: implications for transfer during crenulation cleavage development in the Moretown Formation, western Massachusetts, *J. Struct. Geol., 23*, 923-939.

Wilson, B., T. Dewers, Z. e. Reches, and J. Brune (2005), Particle size and energetics of gouge from earthquake rupture zones, *Nature*, *434*, 749 - 752, doi:10.1038/nature03426.

Zoback, M., S. Hickman, and W. Ellsworth (2010), Scientific drilling into the San Andreas Fault Zone, *Eos Trans. AGU*, *91*(22), 197-204.

Zoback, M., S. Hickman, and W. Ellsworth (2011), Scientific drilling into the San Andreas Fault Zone—An overview of SAFOD's first five years, *Scientific Drilling*, doi: 10.2204/iodp.sd.11.02.2011.

APPENDIX A

COMPOSITE ELEMENT MAPS

The following outlines the methods implemented to create the composite element maps that are used in this study to separate mineral phases for the particle size distribution (PSD) analyses and to define the shape characteristics.

A.1. Creating the Composite Element Map

Each composite element map is based on twelve single-element (Al, Ba, Ca, Fe, K, Mg, Na, P, Si, Sr, Ti, and Zr) X-ray maps and one back-scattered electron (BSE) image of the map area. From these, eight X-ray maps of the most abundant elements (Al, Ca, Fe, K, Mg, Na, P, and Si) are combined with the BSE image to create the composite element map using ImageJ. The grayscale values (0-255), displayed in the single-element X-ray maps, correspond to element abundance. The bright areas (values closer to 0) correspond to regions containing a relatively high concentration of the analyzed element.

A.1.1. Binary Images from Element Maps

To create a binary image of a single element map, the following steps are taken:

1. From the file menu select *Image-Adjust-Threshold*
2. Set both the upper and lower threshold scroll bars to 255.
3. Using the top threshold bar, decrease the threshold value by two histogram increments and click *Apply*.

4. For most cases, the element represented by bright pixels in the original X-ray map should be black in the thresholded image. If not, and instead the originally bright element pixels are white, the image must be inverted. To do this, select *Edit-Invert*.
5. To make the image binary, select *Process-Binary-Make Binary.*
6. Repeat for all eight X-ray maps.
7. The BSE image is used to define regions of epoxy. Threshold the BSE image so that the epoxy is black and everything else is white. The easiest way to do this is to open a duplicate image (*Image-Duplicate*) to track the epoxy and then threshold the original image. Remember to select *Process-Binary-Make Binary* after thresholding.

A.1.2. Creating the Grayscale Composite Element Map

1. The black pixels in each binary image, which indicate the presence of a particular element or epoxy (BSE image), need to be assigned representative grayscale values in order to distinguish individual elements after the images are stacked together to create the composite map. To do this, open the binary images and, one at a time, select *Process-Math-Subtract*. Input the value that corresponds to the element being processed, as indicated by the following: Mg (254), P (253), Al (251), Fe (247), Si (239), Ca (223), Na (191), K (127), and BSE (0). The pixel values (white, black) of the output binary images are as follows: Mg (0,1), P (0,2), Al (0,4), Fe (0,8), Si (0,16), Ca (0,32), Na (0,64), K (0,128), and BSE (0,255).

2. Next, the subtracted binary images are added together to create a grayscale composite map. The value of each pixel composing the composite map is the sum of all pixel values for the elements present at that location. Therefore, every pixel value represents a specific element combination, which is used to interpret the existing mineral phases.
    a. Open two of the subtracted, binary element maps. To keep track of the following steps, it is easiest to start with the lowest value binary images (Mg and P) and work in sequential order.
    b. Select *Edit-Paste Control* and choose *Add* from the drop down *Transfer Mode* box.
    c. Using either the *box tool* or *ctrl-a,* select the entire Mg element map area and select *Edit-Copy* or click *ctrl-c.*
    d. Activate the P element map window and select *Edit-Paste* or click *ctrl-v.* This will add the two maps together. Save this new image as *Mg+P*. It is important to save a new image file each time an element is added. If another image is added without saving, a glitch in the program results in inaccurate pixel values.
    e. Close the Mg and P windows. Keep the *M+P* image open and repeat steps c and d for the 6 remaining subtracted binary images and the subtracted BSE image.

A.2. Composite Element Map Interpretation

A.2.1. Mineral Phase Determination

The composite element maps are interpreted using a spreadsheet (Table 6) that displays 255 possible numeric combinations of the gray values assigned to each element map (1, 2, 4, 8, 16, 32, 64, and 128). The *Pixel Gray Value* column lists the possible total pixel values from 0 to 255 that result by summing different combinations of elements. The *Numeric Combination* column shows the combination of pixel values that would sum to equal the adjacent total pixel value. The *Element Combination* column lists the elements that correspond to the neighboring numeric combination values. The steps to interpret the data using this spreadsheet are as follows:

1. Return to ImageJ and open the composite element map.
2. Select *Analyze-Histogram* and click on the *List* button at the bottom of the histogram window.
3. The *List* window contains two columns: *value* and *count*. The *value* column lists all pixel values from 0 to 255 and the *count* column shows the number of pixels that correspond to each adjacent pixel value. Copy the *count* and *value* columns and paste them into the spreadsheet so that the first count value lines up with the pixel gray value of 0. The *value* column is the same as the *Pixel Gray Value* column and therefore can be deleted.
4. Use the number of counts to determine which numeric/element combinations are most abundant. Start by looking at the element combinations for counts greater

than or equal to 1000. Study each combination of elements and interpret/assign the matching mineral phases.

A.2.2. Color Indexing the Composite Element Map

After identifying the abundant mineral phases, a color is assigned to each gray value that represents a certain mineral. This allows easy identification of minerals in the composite map and can be done in ImageJ by the following:

1. Open the grayscale composite element map.
2. Select *Image-Color-Edit LUT*.
3. The lookup table (LUT) window contains 256 boxes with gray values from 0 to 255. To assign a color, find the box equal to the gray value of one mineral and click on that box. A new window appears that allows the RGB color values to be adjusted. Change the values to get a desired mineral color and click *OK*. Repeat this for the remaining mineral phases.
4. Before closing the LUT window, click *Save* and create a file name for the new LUT. This will allow the modified LUT to be reopened and applied to other composite maps collected in regions of similar composition, which may only require minor adjustments to the previously created LUT.

APPENDIX B

PARTICLE SIZE AND SHAPE ANALYSIS

The following outlines the procedures employed to quantify particle size and shape as a function of mineralogy using backscattered electron (BSE) images, composite element maps, and image processing software.

B.1. BSE-Composite Element Map Overlay

Each overlapping set of five to eight backscattered electron images are merged together using Adobe Photoshop (*File-Automate-Photomerge*). The panoramic BSE images and composite element maps are overlain for phase specific grain boundary determination. The composite maps with a 2 µm pixel size are superimposed on the low magnification BSE images (150X and 600X; Figure 17) and the composite maps with a ¼ µm pixel size are superimposed on the high magnification BSE images (2400X and 9600X). This can be done in Adobe Photoshop as follows:

1. Open the merged BSE image and corresponding element map in Adobe Photoshop.
2. Select the BSE file window and click *Image-Mode-RGB color*. Changing the image mode from grayscale to color allows the composite map to retain the color-indexed minerals when it is brought in.
3. The resolution of the panoramic BSE image is 136 pixels/cm and the panorama consists of 5 to 8 overlapped BSE images with pixel dimension of 2048 x 1887.

Comparatively, the resolution of the composite map is 28.35 pixels/cm and the pixel dimensions are typically 512 x 512 (1 x 1 mm, 2 μm per pixel map). Because of the differences in resolution and pixel dimension, it is necessary to change the scale of the composite map before it is pasted onto the BSE panorama. Select the composite map file window, click *Image-Image Size,* and change the pixel dimensions to 2048 x 2048. Click *OK*.

4. Select the composite map using either *ctrl-a* or the *Rectangular Marquee Tool* and click *Edit-Copy.*
5. Select the BSE file window and click *Edit-Paste*. The layer window should show two separate layers containing either the BSE image or the composite map (to make the layer window visible, select *Window-Layer*). If not, and the composite map is in the same layer as the BSE image, delete the composite map, create a new layer (*Layer-New-Layer)* and then re-paste the map.
6. In the layer window, change the opacity to 50% for the composite element map layer.
7. Select the *Arrow Tool* and align the composite map with the BSE image. To create a more accurate alignment, select *Edit-Free Transform*. Use this tool to apply small size and orientation changes to the composite map until the superposed images are aligned.
8. Next, select *Layer-Layer Style-Blending Options* and change the *Blend Mode* box to *Multiply*. The multiply blend mode enhances grain boundaries and fractures.

B.2. Grain Outlines

Grain boundaries are digitized using a Wacom Bamboo Digitizing Tablet. The following steps are repeated for all three mineral phases (quartz, orthoclase, and quartz).

1. Create a new layer (*Layer-New-Layer*), ordered above the composite map and BSE image, in the layer window. Select this layer.
2. Select the *Pencil Tool* and change the *Brush Diameter* to 2 pixels. Single pixel brush diameters should not be used to separate grains because diagonal lines drawn to separate two particles will leave particles connected by the corners of pixels steps. As a result ImageJ will view these particles as one grain during the automated analysis.
3. Choose a color from the swatches window (*Window-Swatches*) that will stand out against the composite map. Next, systematically traverse the BSE-composite map and trace all of the visible grains of a single mineral phase.
4. Select the *Line Tool*. Use this tool to draw a line on the grain outline layer that is equal to the length of the scale bar shown on the BSE Image. Employ the *Horizontal Type Tool* to record the length of the scale bar. Divide the length of the scale bar in pixels by the length of the scale bar in microns to get a pixel per micron value that will be used later to convert the output data to microns.
5. Save everything to this point as a separate file. The layer showing the grain outlines will be modified in the following steps. It is good to have a file with the original grain outlines for ease of editing.

6. After saving as a separate file, delete the BSE and composite map layers. Leave the grain outline layer.
7. Create a new layer. Make sure it is ordered below the grain outline layer in the layer window. Select the *Paint Bucket Tool* and color the layer white. Then right mouse click the layer and select *Merge Layers*. This will merge the grain outline layer with the white background.
8. To turn the grain outlines black, select *Image-Adjustments-Replace Color*. Select the *Eyedropper Tool*, and click the grain outline. Then set the *hue* to -180, the *lightness* to -100, and the saturation to -100. The grain outlines should now be black. Click *OK*.
9. The particles need to be filled in with black for the automated particle analysis. To do this, select the *Paint Bucket Tool* and choose black from the *Swatches* window. Color the white background black leaving all the grains white and then click *ctrl-z* or *Edit-Undo*. Repeat this step several times and watch each time to see if any particles disappear when the background is colored black. If a particle disappears, it has a discontinuous grain boundary. Locate and fix the space or spaces in the grain boundary before proceeding to the next step.
10. Once the background is black and all of the particles are white, select *Image-Adjustments-Invert*. Now the particles should be black, floating in a white background.
11. Change the image to *8-bit*, *grayscale* by selecting *Image-Mode*. This is the best format for opening the image in ImageJ.

12. Save the image as a tiff file.

B.3. Image Area Measurement

It is necessary to normalize the cumulative number of particles captured at each magnification by the image area. The image area values are entered in the *Global Variables-Areas (mm^2)* cells, which are referred to later in this appendix. The steps used to calculate image area include:

1. Particles that intersect the edge of the image area are not considered in the particle size analysis. Therefore, these particles should not be considered in the total image area. Open the file showing the particle outlines. This file should include the outline layer with scale bar, element composite map layer, and BSE layer.
2. Create a new layer and order it first in the layer window. Then, using the *Line Tool*, replicate the scale bar from the outline layer. Order this scale bar-*shape layer* over the new layer in the layer window. Then, delete the outline layer.
3. Make sure the new layer is highlighted in the layer window. Using the digitizing tablet, *Pencil Tool*, and a black, 2-pixel-wide line, outline all grains contacting the edge of the image. Record all mineral phases cut-off at the edge of the image in this one layer. All of the phases contacting the edge of the image will be subtracted from the total image area simultaneously.
4. After all the edge grains are outlined, delete the composite map and BSE image.

5. Click the *eye* in the layer window, next to the scale bar-*shape layer,* to turn off the layer.
6. Select *Layer-New-Layer*. Make sure the new layer is ordered last in the layer window. Select the *Paint Bucket Tool* and color the layer white. Then right mouse click the layer in the layer window and select *Merge Visible Layers*. This will merge the edge grain outline layer with the white background.
7. Color the white background black, leaving all the edge grains white.
8. Turn on the scale bar layer and change the line color to white so it is visible against the black background.
9. Save as a tiff file.
10. Complete steps 1-9 from the next section of the appendix (Quantification of Particle Size and Shape) with the following adjustments to steps 4, 7, and 9.
    a. Step 4: This step is not necessary if the scale bar is wholly contained within the black background. Before the analysis is run (step 8e), the *Include Holes* option is selected, which treats any white area contained within a black particle as part of the total area.
    b. Step 7: The only measurement box that needs to be selected from the *Analyze-Set Measurements* menu is *Area*.
    c. Step 9: Use the output *Drawing* window to make sure that the only object outlined is the image area minus the edge grains. If this is the case, there should only be one area value in the *Results* window. This is the desired image area in pixels^2. The previously determined pixel per micron value

is used to find the image area in microns by dividing the image area in pixels^2 by the pixel per micron value squared.

B.4. Quantification of Particle Size and Shape

Automated particle size and shape measurements, and calculations are completed in ImageJ and Microsoft Excel (Table 7) using the following methods:

1. Open the tiff file in ImageJ.
2. Select *Image-Properties* and change the *Unit of Length* to pixels. Then change the *Pixel Width, Pixel Height,* and *Voxel Depth* to one. Select *Global* and click *OK*.
3. The *Straight Line* tool can be used as a measurement tool. Select the *Straight Line* from the tool bar and use it to draw a line of equal length to the scale bar at the bottom of the image. The pixel length of the new line will appear in the blank space just below the icons in the tool bar. Record this number. This is used later to convert areas recorded in pixels to microns.
4. Select the *Rectangle Tool* from the tool bar, draw a box around the scale bar line, and push delete. If the scale bar is not deleted, it will be measured and recorded as a particle during the automated analysis. To get rid of the rectangle, select *Edit-Selection-Select None*.
5. The image should already be an 8-bit image. If it is not, select *Image-Type-8-bit*.
6. Before the image can be processed, it needs to be converted to a binary image. To do this, select *Process-Binary-Make Binary*.

7. Prior to running the automated analysis, the output parameters need to be set. Click *Analyze-Set Measurements* and check the boxes in front of *Area*, *Shape Descriptors*, *Perimeter,* and *Fit Ellipse.* For this study, these are the only boxes that should be selected. Keep the default inputs for the *Redirect to* box and the *Decimal places* box. Select *OK*.
8. Now the automated particle size and shape analysis may be completed. To do this, select *Analyze-Analyze particles*.
    a. The *Size (pixels^2)* range may be changed, but is kept at *0-Infinity* for this study.
    b. Check the box next to *Pixel Units*
    c. The *Circularity* range may be changed, but is kept at *0.00-1.00* for this study.
    d. Change the *Show* box to *Outlines*.
    e. Check the boxes next to *Display Results*, *Exclude on Edges, and Include Holes* and click *OK*.
9. Two new windows should open: Use the *Drawing of grain outlines* window to make sure the particles have been accurately separated. Save the *Results* window as a tab delimited text file.
10. To calculate equivalent particle diameter, open the *Results* text file in Excel and complete the following steps:
    a. Delete the first, unlabeled column of sequential numbers and the columns labeled *Angle, AR,* and *Round.*

b. Insert six columns in between the *A* (area) and *perimeter* columns.

c. Highlight all data in the spreadsheet: Select *Data-Sort*, choose *Area* from the *sort by* drop down menu, check the boxes next to *Header row* and *Descending* and then click *OK*.

d. Label the first empty column (adjacent to the *Area* column) *d* for particle diameter. Insert *=SQRT(4*A2/pi()) into* cell *B2* and click enter. Fill the series down to the last row of data by double clicking on the bottom right corner of the cell.

e. Label columns *C* and *D*, *A (µm) and d (µm)*, respectively.

f. To convert the area values recorded in pixels to microns, use the previously recorded pixel per micron value and enter *=(A2/(pixel/µm value)^2)* in cell *C2* of the *A* (*µm*) column. Fill the series down to the last row of data.

g. To convert the diameter values calculated in pixels to microns, use the previously recorded pixel per micron value and enter *=B2/(pixel/µm value)* in cell *D2* of the *d* (*µm*) column. Fill the series down to the last row of data.

11. The circularity and solidity values are automatically output by selecting the shape descriptors measurement option before the particles are analyzed. However, elongation is calculated after the analysis using data from the *Major (I)* and *Minor (J)* columns. These columns are the major and minor axes of the best-fit ellipse to the analyzed particle. To calculate elongation insert a new column

adjacent to column *J* and label it *Elongation (*column *K)*. In cell *K2,* enter *=(1-(J2/I2))*. Fill the series down to the last row of data.

12. To calculate the log particle diameter for the log-log cumulative PSD plots use the diameter values recorded in microns (*column D*). Select *column F* and label it Log *d*. In cell *F2,* enter *=log(D2)* and then fill the series down to the last row of data.
13. For the next step, the log cumulative number of particles needs to be calculated for the log-log cumulative PSD plots. To do this:
    a. Select *column E* and label the column *CN* (for cumulative number). Then select cell *E2* and enter *1*. The value of one represents the largest particle, and the fact that this is the only particle of that size or greater, giving a cumulative number of 1. In cell *E3* enter *2*. This corresponds to the second largest particle, and the fact that there are two particles of this size or greater (a cumulative number of 2). In cell *E4* enter *3*. Highlight cells E1to *E*3 and double click on the bottom right corner of the box to sequentially number the series down to the smallest recorded particle.
    b. Next, select *column G* and label the column *Log CN*. In cell *G2* enter *=log(G2)* and fill the series down to the last row of data.

B.5. Particle Size Distribution (PSD) Plots

The final log *d* verses *C(d)* plots are created using a PSD normalization spreadsheet created to bin the size data and normalize the cumulative number of particles

recorded per magnification by the image area at that magnification. The following steps are taken from the PSD normalization spreadsheet. An example portion of this spreadsheet is shown in Table 7.

1. Global variables (Blue cells)
    a. Areas (mm^2): Image area (mm^2) analyzed at each magnification is needed to calculate *Log Cumulative Number per Area (#/mm^2).* Enter these previously calculated values (Appendix B.4.) for each magnification.
    b. Area shift factor: If needed, an additional (subjective) shift can be made at magnification, after applying the true area correction, to best align the 150X, 600X, 2400X, and 9600X curves with the 50X data. This step is explained in greater detail in the "Chart for Shift" section of the appendix.
    c. Plot increment: Insert the desired bin increment for *Log d*. Note: If the *increment, shift factor, or area,* is changed during the analysis, the data in the yellow columns will need to be re-entered (see note below in step 5). The plot increment used in this study is 0.05.
2. Data Columns (White cells): The following two steps are applied for the 50X, 150X, 600X, 2400X and 9600X data sets:
    a. Copy raw data for *Log d (mm)* from the spreadsheet used to calculate particle diameter (e.g. Table 7) and paste special as values into appropriate columns labeled *Log d (mm)*.

b. Copy raw data for *Log CN* (e.g. Table 7) and paste special as values into appropriate columns labeled *Log CN.*

3. Binned Data Columns (Green cells): The *bin log d* column bins the *Log d (mm)* data according to the *Plot increment* entered in the *Global Variables* column. The *bin log d (mm)* column converts the *bin log d* data, given in µm, to *bin log d* data expressed in mm, and the *log norm #* column normalizes the *Log CN by the Area (#/mm^2)* entered in the *Global Variables Column.*

    a. After entering data into the white columns, fill down the formulas in row 2 in the three green columns by selecting the three green cells in row 2 and double clicking in the lower right corner of the right cell. The three green columns should all fill with the expression, *#VAULE!,* down to the last row of data in the white columns. The green columns below this row should remain blank.

    b. To get the green columns to fill with numerical values, for a *Plot increment* 0.05, look at the *bin log d (mm)* value in D2 and type the appropriate incremented *bin log d value* (in mm), corresponding to this value, in F2. That is, if D2 is 2.65098 (Table 8), then the *bin log d value for F2* is the 0.05 increment just below that value (i.e., 2.65). Immediately change the font color of the F2 value to red to indicate that this was a manually entered value. Once 2.65 is entered, hit return. The green columns may all fill down with numerical values. If they do not, then go

to the next empty cell in column *F* and repeat the steps, remembering to make the font red for all manually entered values.

4. Chart for Shift (Figure 18):
    a. Initially, this sheet presents a plot of all binned data for each magnification, corrected for the areas analyzed. Use this chart to decide which data sets need further shifting (Figure 18a).
    b. The 50X data should not be shifted, i.e., the shift factor should remain unchanged.

        1. To determine shift value for 150X, compare the overlapping portions of the 50X and 150X curves. For a particular x-value, take the difference between the two y-values (*D[log cum #/area]*) and solve for *D cum #/area* (i.e., the shift factor). Enter this value as the shift factor for 150X into the appropriate *Global Variables* column. Repeat this procedure for the 600X, 2400X and 9600X data sets if necessary. After the shift factors are entered, a modified plot is produced that will represent the area-normalized and shifted data (Figure 18b).

5. Sorted Data for Plotting (Yellow Columns):

    Note: If you change any of the *Global Variables* in the blue shaded column, this will change the values in the green columns; therefore you must re-copy and re-paste the recalculated data into the yellow columns and re-sort.

a. Copy the middle and right-most green columns for each magnification (*bin log d (mm)* and *log norm #*) and paste special as values into the neighboring yellow columns.

b. While these two columns are still highlighted, sort the yellow columns with respect to *log norm#* (i.e., Data-Sort-column *J*, ascending order, with Header row checked). This sorting puts all empty cells (i.e, all zero-values) at the end so they are not plotted.

6. Normalization Sheet – Plot (Figure 19a): This graph presents all area-normalized-shifted data (i.e., data from the yellow columns). To plot selected data on this graph:

    a. First make sure that all data from the yellow columns are plotted for each magnification. To determine this, click on graph, click on a point from one of the data sets and go to appropriate yellow columns and grab the upper or lower blue toggle and encompass the desired data. Do this for each data set.

    b. Now looking at all plotted-incremented data, pick appropriate upper and lower cut-offs for the 150X and 600X data sets, a lower cut-off for the 50X data set, and an upper cut-off for the highest magnification data set (2400X or 9600X). Using the blue toggles, select the points to be represented on the plots based on these cut-offs (Figure 19b).

APPENDIX C

FIGURES AND TABLES

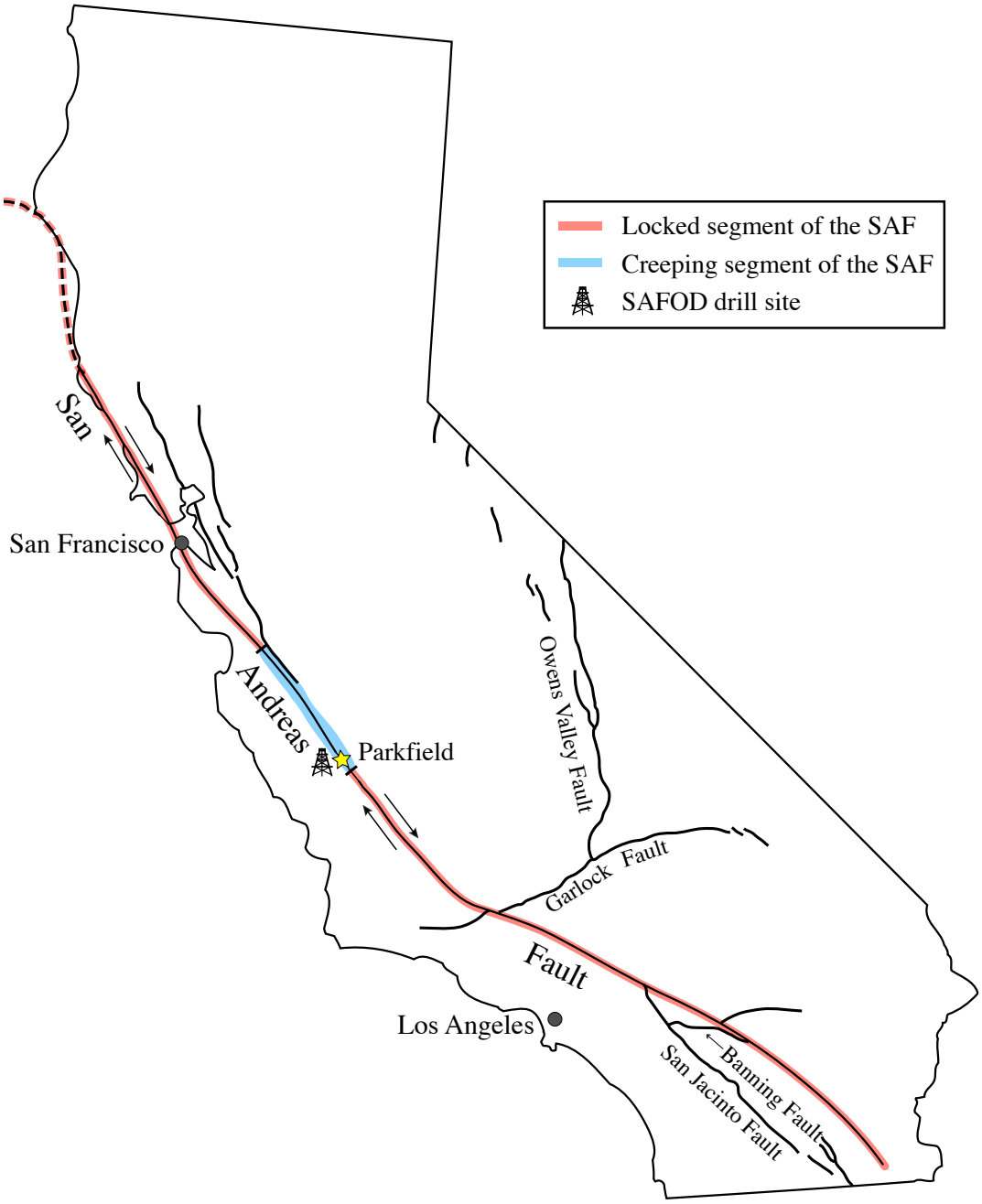

Figure 1. Map of California showing the locations of creeping and locked sections of the SAF and the SAFOD drill site. Modified from Watson [1997].

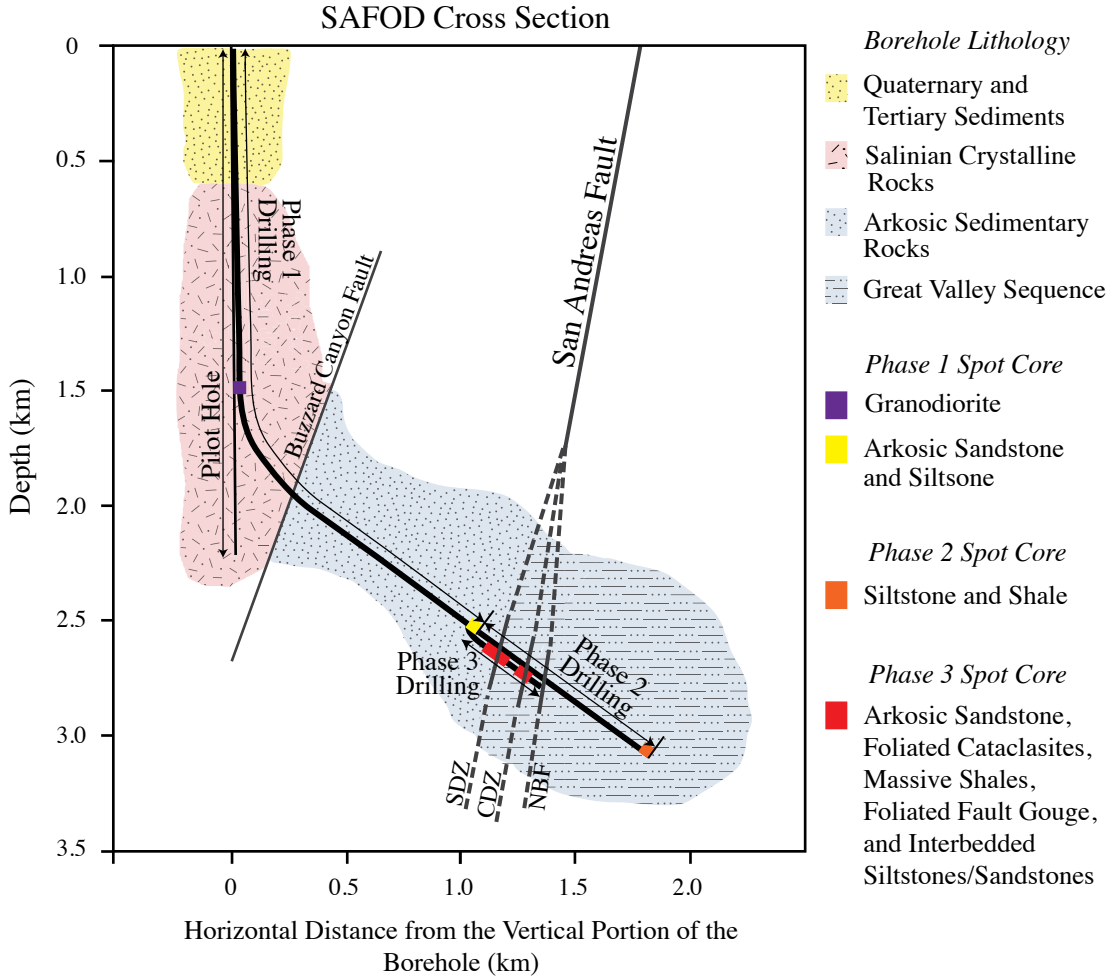

Figure 2. Cross section illustrating the SAFOD borehole, geologic units intersected by drilling, and cored intervals. The main borehole was completed in three phases of drilling. Spot coring during Phase 1 in 2004 recovered a total of 7 m of granodiorite, and 12 m of arkosic sandstone, siltstones, and shales from the western damage zone. In 2005, Phase 2 drilling and coring produced a suite of 70 sidewall cores through the fault zone, and 3 m of siltstone and sandstone at the very base of the borehole. In 2007, during Phase 3, two multilateral holes were completed off the main borehole. Spot coring during Phase 3 retrieved 11 m of arkosic sandstones, siltstones, and shales from the western damage zone, 13.6 m of siltstones, shales, cataclasites, and gouge associated with the Southwest Deforming Zone (SDZ), and 17.1 m of siltstones, sandstones, and gouge from the Central Deforming Zone (CDZ). Samples used in this study are from the arkosic sandstone, retrieved during Phase 1 (yellow box), that are ~130 m west of the actively creeping SDZ. The Northwest Bounding Fault (NBF) also is shown. Cross section modified from Chester et al. [2008] and Sills [2010].

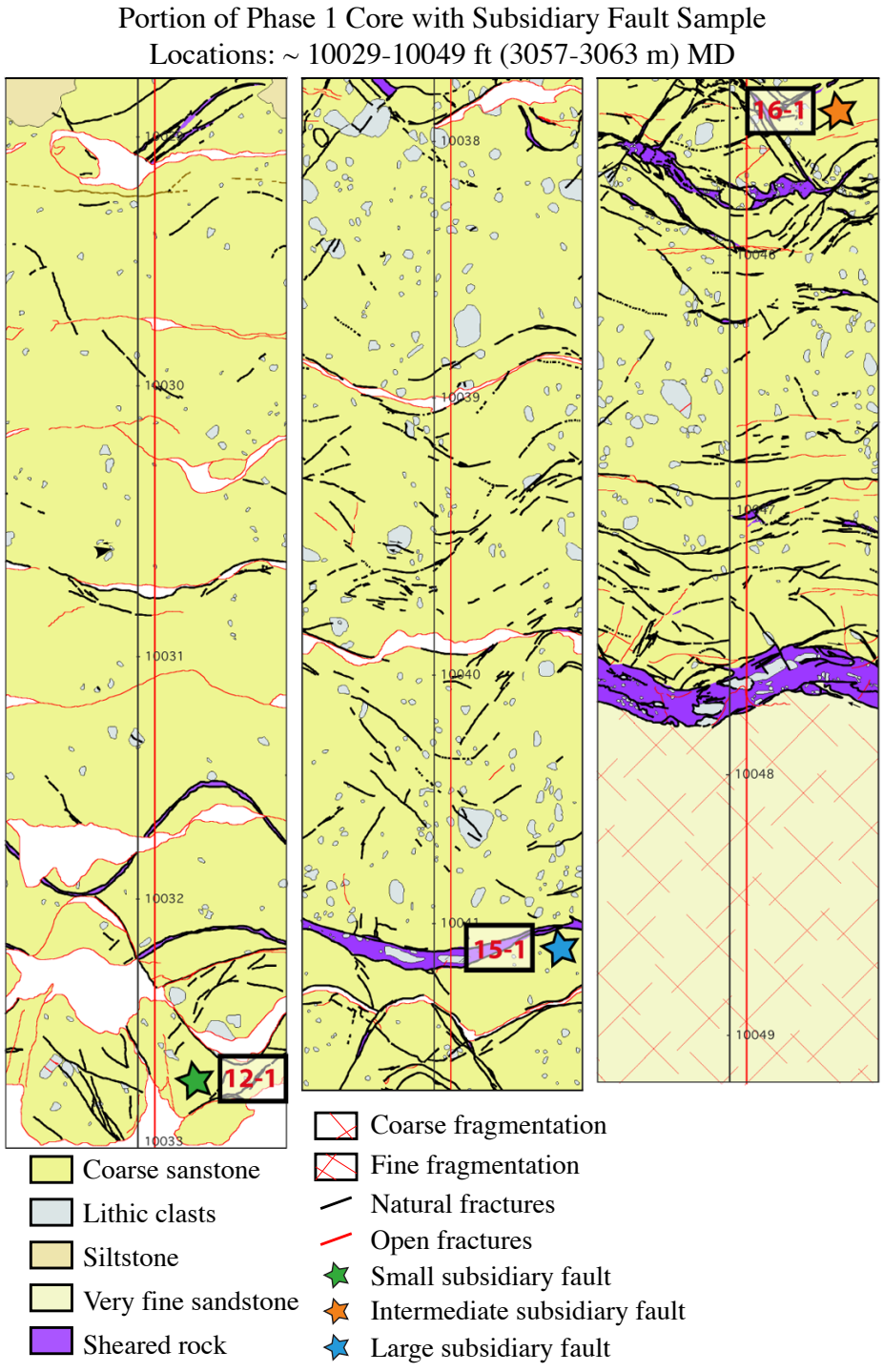

Figure 3. Wrap around maps of the arkosic sandstone, siltstone, and shale spot core from Phase 1, showing mesoscale fractures and faults. The three subsidiary faults used in this study are indicated by a star and box around the sample number. Figure modified from Almeida [2007].

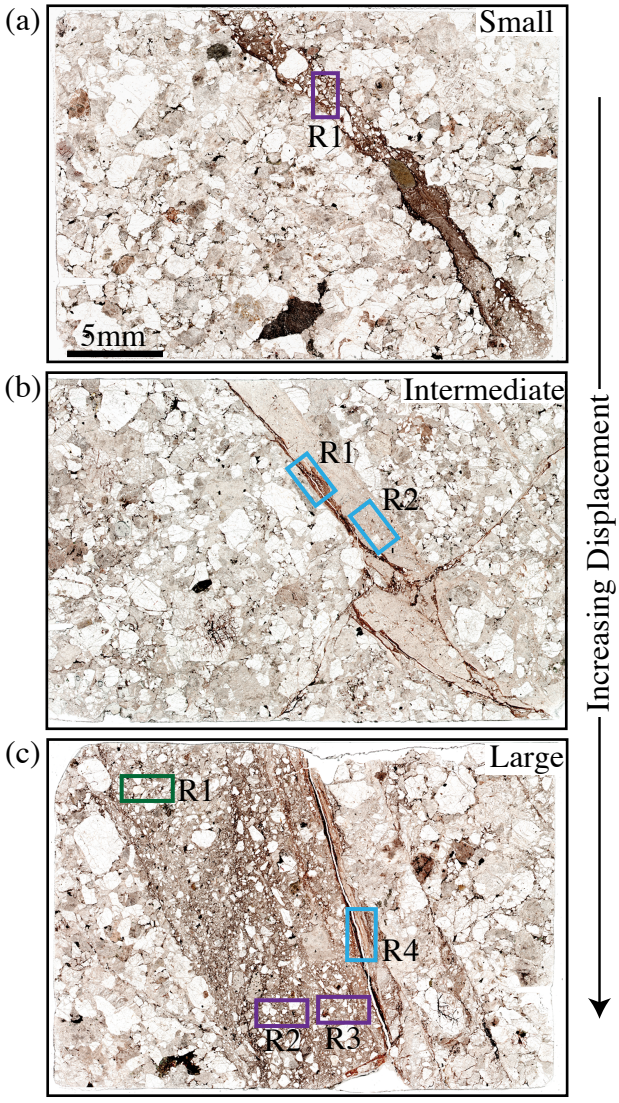

Figure 4. Plane light images of the three subsidiary faults used in this study. Boxes show regions (R) analyzed. Colors correspond to distinct structural units: brecciated sandstone (BSS; green), microbreccia (MB; purple), and microbreccia within a distinct shear zone (MBS; blue).

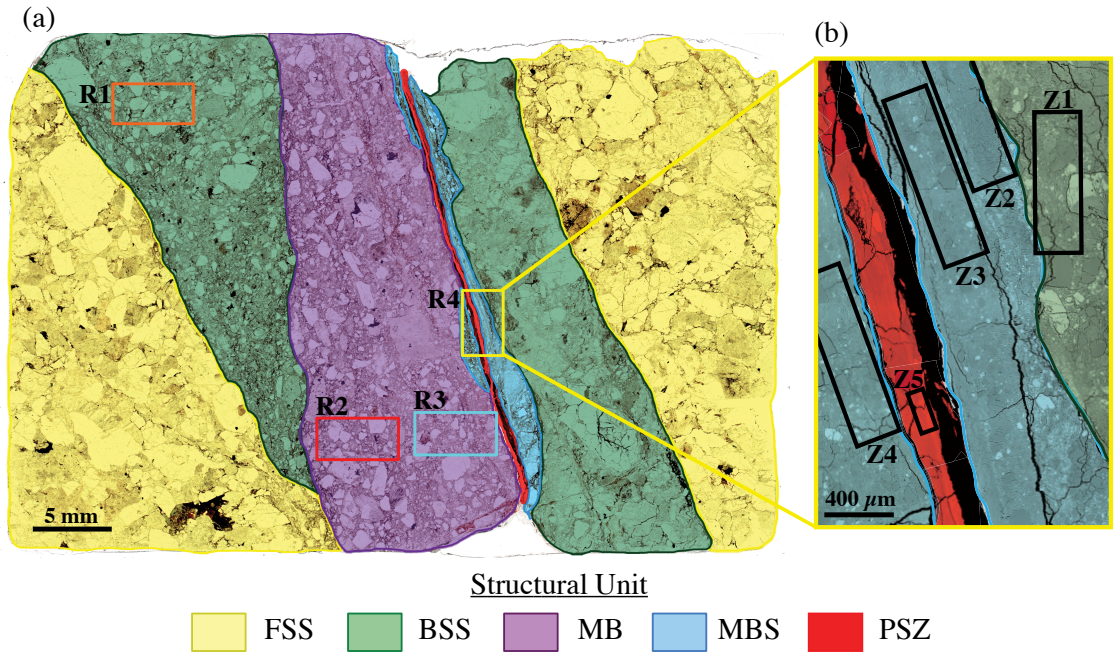

Figure 5. Plane light and BSE images of the large subsidiary fault. (a) Plane light image showing the five distinct structural units distinguished by color. Boxes outline representative regions (R) studied. (b) A BSE image of Region 4 at higher magnification indicating the specific zones (Z) within this region analyzed in detail.

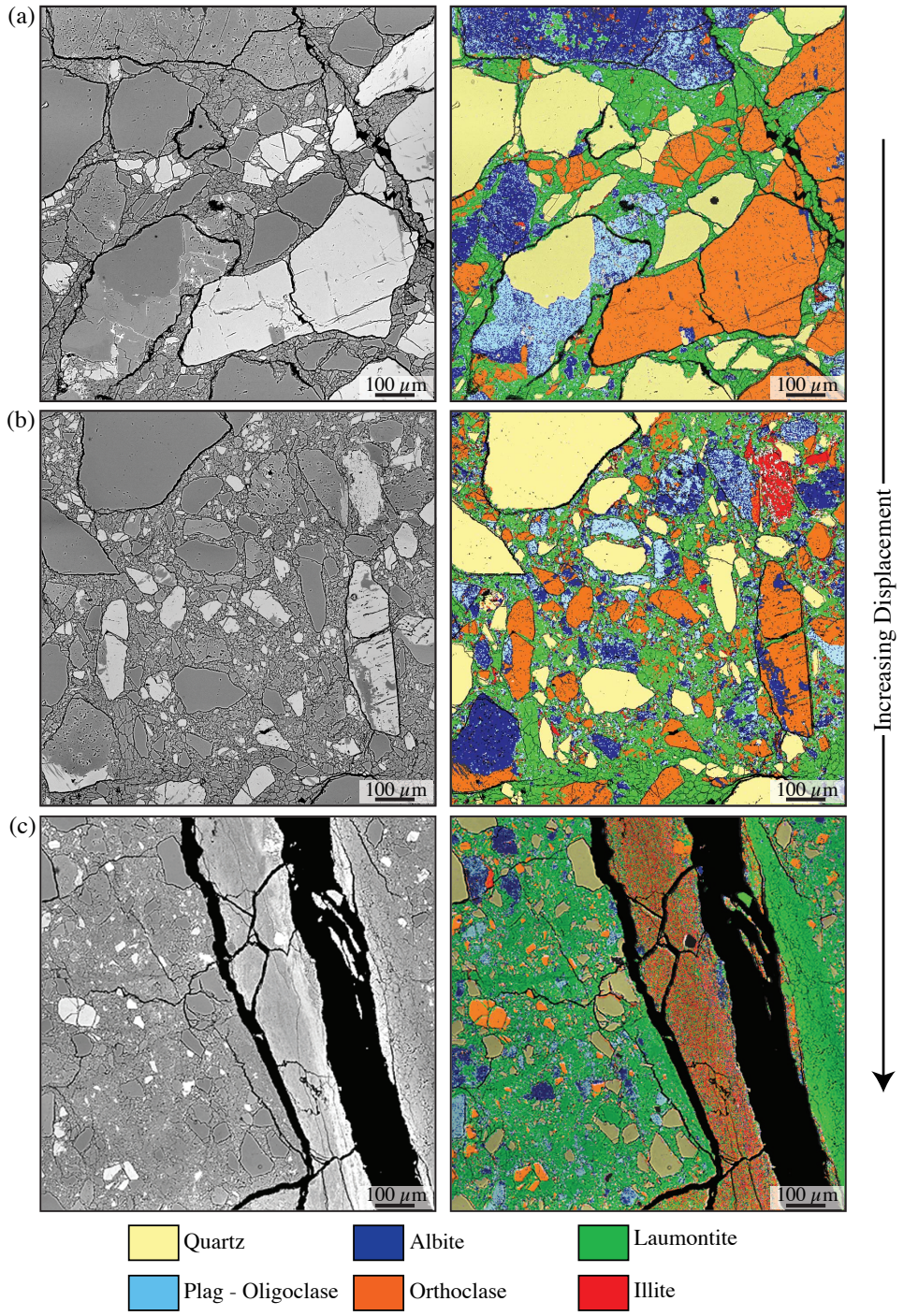

Figure 6. BSE images and corresponding composite element maps illustrating variations in mineralogy, microstructure, and particle size for different structural units. (a)-(c) BSE images and composite element maps overlaying these BSE images for the BSS (a), MB (b), and MBS (c). Colors correspond to different mineral phases as indicated in key. (d) Plane light image of the FSS.

(d)

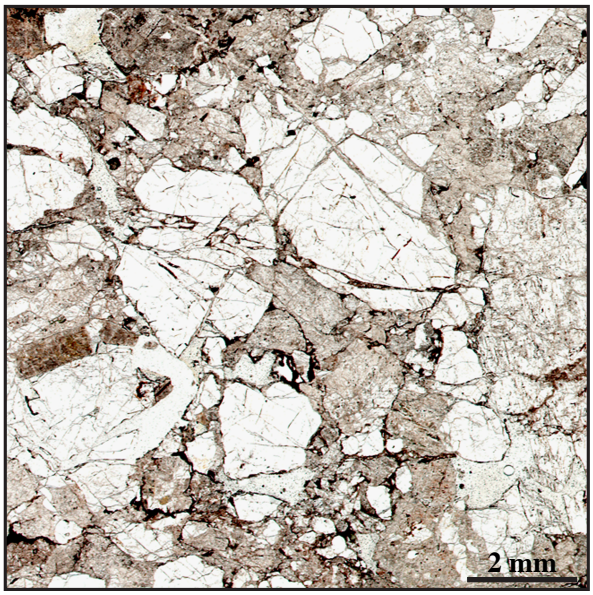

Figure 6. Continued

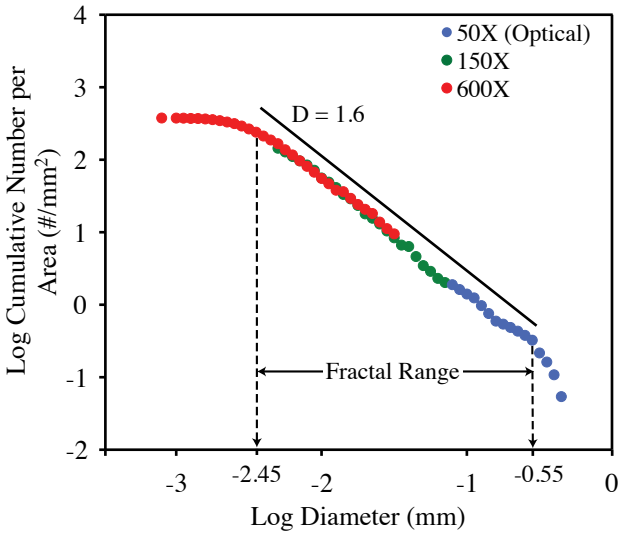

Figure 7. Example of a composite PSD plot for a single mineral phase, showing upper and lower cut-offs used to determine best-fit D. Data are plotted as log cumulative number per area versus log particle diameter. Colors distinguish data collected at three magnifications. The cumulative number of particles recorded for each magnification is normalized by the area analyzed at that magnification. Vertical dashed lines mark the upper and lower particle-size cut-offs used for fitting the power law. Slope of the best-fit line and D are shown. Data shown are for orthoclase from the MB (Region 2) of the large subsidiary fault.

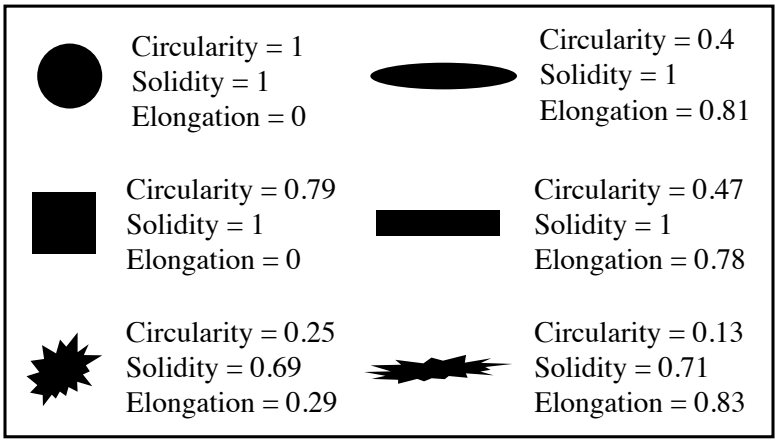

Figure 8. Example values of circularity, solidity, and elongation for different particle shapes. Circularity describes the overall form and surface roughness of a particle, whereas solidity values only distinguish changes in surface roughness. Elongation describes the overall form of a particle, but gives no indication of surface roughness. Figure modified from Crompton [2005] and Bjork et al. [2009].

Table 1. Area Fraction (%)[a] of Mineral Phases Analyzed for Each Structural Unit[b]

Phase	BSS	MB	MBS
	With Laumontite		
Albite	16.09	14.95	7.28
Oligoclase	10.62	12.41	7.52
Orthoclase	27.10	21.83	7.96
Quartz	23.41	21.95	10.81
Laumontite	22.78	28.87	66.44
	Excluding Laumontite		
Albite	20.84	21.01	21.69
Oligoclase	13.75	17.44	22.40
Orthoclase	35.09	30.69	23.71
Quartz	30.32	30.86	32.20

[a]Excludes area occupied by accessory minerals (2% to 8% of total imaged area)

[b]BSS, brecciated sandstone; MB, microbreccia; MBS, microbreccia with shears

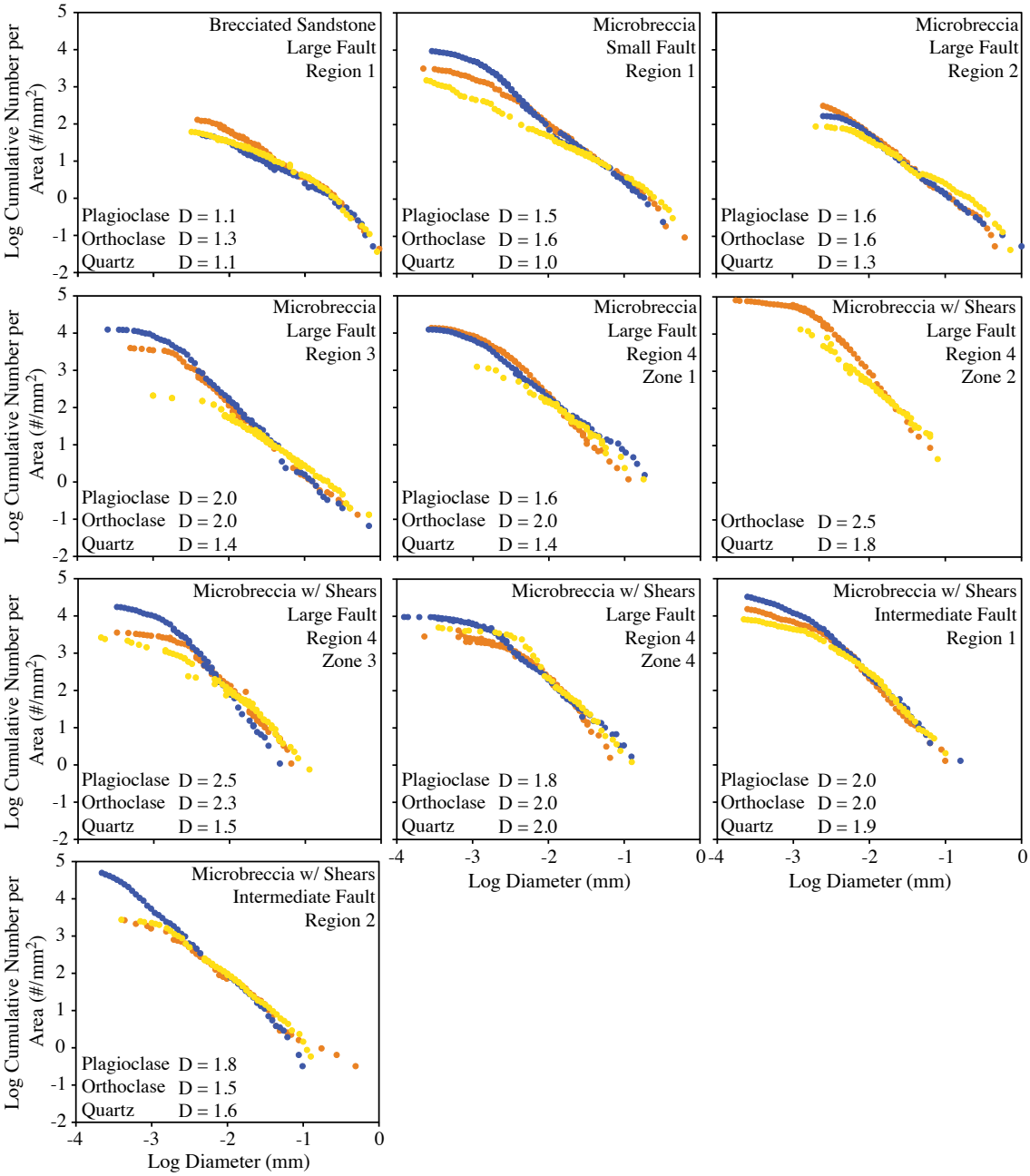

Figure 9. Composite PSD plots for all regions analyzed in the three size-classes of subsidiary faults separated by structural unit and mineral phase. Data are plotted as log cumulative number per area versus log particle diameter. Data for all magnifications analyzed are combined for each mineral (see Figure 7 for details). Orthoclase is shown in orange, plagioclase in blue, and quartz in yellow. The best-fit D is indicated.

Table 2. Summary of the Particle Size Ranges used in the PSD Analysis and the Calculated Fractal Dimension Values[a]

Fault	Sample	Structural Domain	Mineral[b]	D	Particle Size Range (μm)		Power Law Cut-offs (μm)		Average D
					Upper	Lower	Upper	Lower	
Small	R1	MB	Plagioclase	1.5	251	0.2	158	1	
			Orthoclase	1.6	630	0.2	178	2	1.3
			Quartz	1	1120	0.2	178	0.5	
Large	R1	BSS	Plagioclase	1.1	620	3	200	6	
			Orthoclase	1.3	815	3	200	8	1.1
			Quartz	1.1	895	3.4	252	5.5	
Large	R2	MB	Plagioclase	1.6	562	2.5	316	5.5	
			Orthoclase	1.6	446	2.5	381	5.5	1.4
			Quartz	1.3	891	2.5	398	8	
Large	R3	MB	Plagioclase	2	708	0.25	200	1.7	
			Orthoclase	2	501	0.5	158	2	1.7
			Quartz	1.4	1122	1	312	6	
Large	R4, Z1	MB	Plagioclase	1.6	141	0.2	112	1	
			Orthoclase	2	112	0.28	112	2	1.6
			Quartz	1.4	178	0.7	89	4	
Large	R4, Z2	MBS	Plagioclase	-	-	-	-	-	
			Orthoclase	2.5	32	0.2	32	1	2.1
			Quartz	1.8	80	1.2	63	3	
Large	R4, Z3	MBS	Plagioclase	2.5	35.5	0.2	35	1	
			Orthoclase	2.3	50	0.25	45	2	2
			Quartz	1.5	126	0.2	40	3	
Large	R4, Z4	MBS	Plagioclase	1.8	89	0.2	89	1	
			Orthoclase	2	50	0.5	22	3.5	1.8
			Quartz	2	125	0.8	125	9	
Int.	R1	MBS	Plagioclase	2	126	0.2	45	1.2	
			Orthoclase	2	80	0.2	80	2	2
			Quartz	1.9	100	0.2	70	3	
Int.	R2	MBS	Plagioclase	1.8	89	0.2	28	0.3	
			Orthoclase	1.5	447	0.4	32	2	1.7
			Quartz	1.6	126	0.4	89	1.5	

[a]Int, intermediate; BSS, brecciated sandstone; MB, microbreccia; MBS, microbreccia with shears
[b]Plagioclase refers to the combined data set for albite and oligoclase

(a)

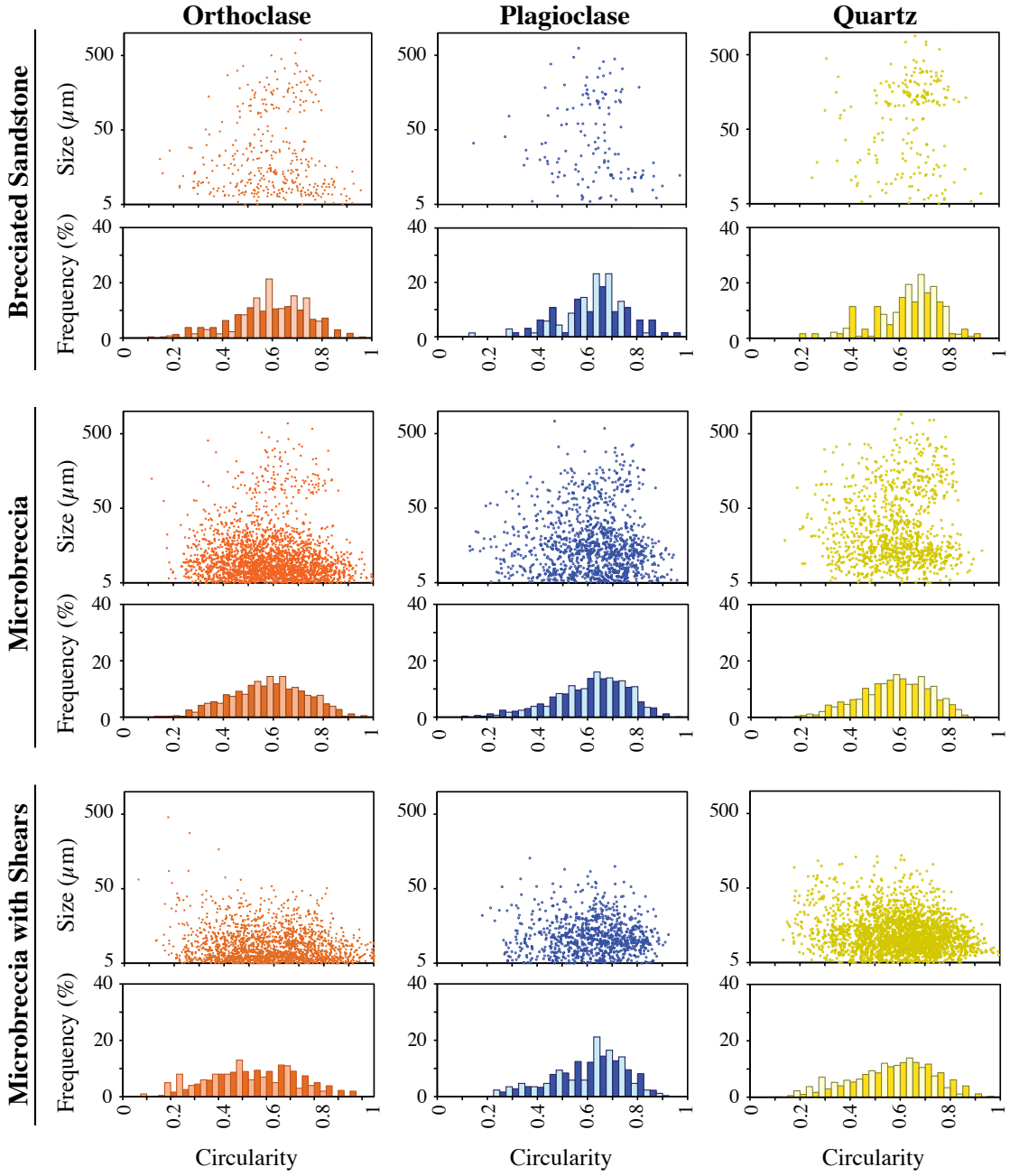

Figure 10. Scatter plots of the three shape descriptors versus particle diameter, and histograms showing the frequency distribution of the shape descriptor, for the individual mineral phases as a function of increasing shear strain. The clustered-column frequency distributions are plotted for two particle size bins. The light colored columns represent the large particle-size fraction (> 25 μm) and the dark colored columns represent the small particle-size fraction (5 to 25 μm). Plots show data for (a) circularity, (b) solidity, and (c) elongation.

(b)

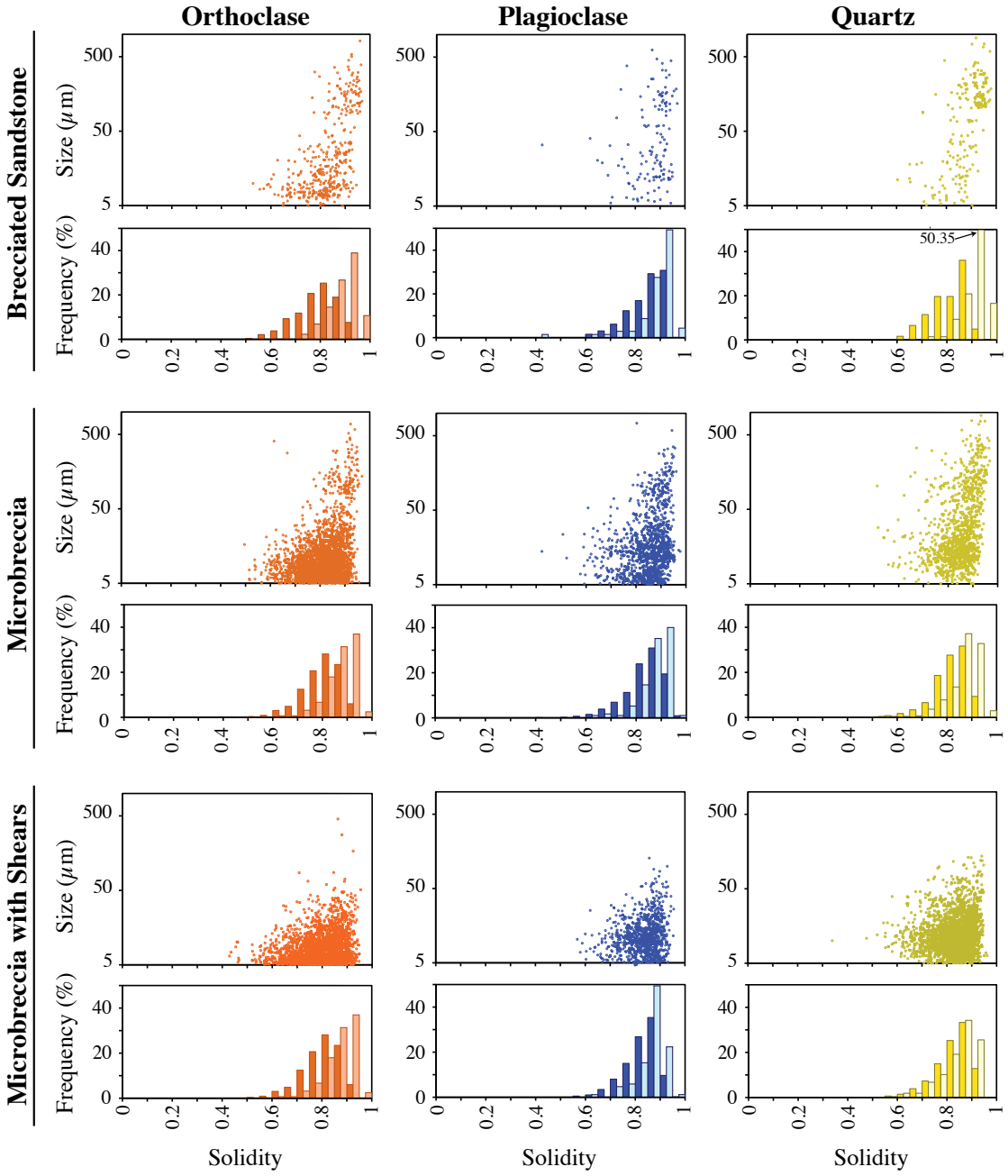

Figure 10. Continued

(c)

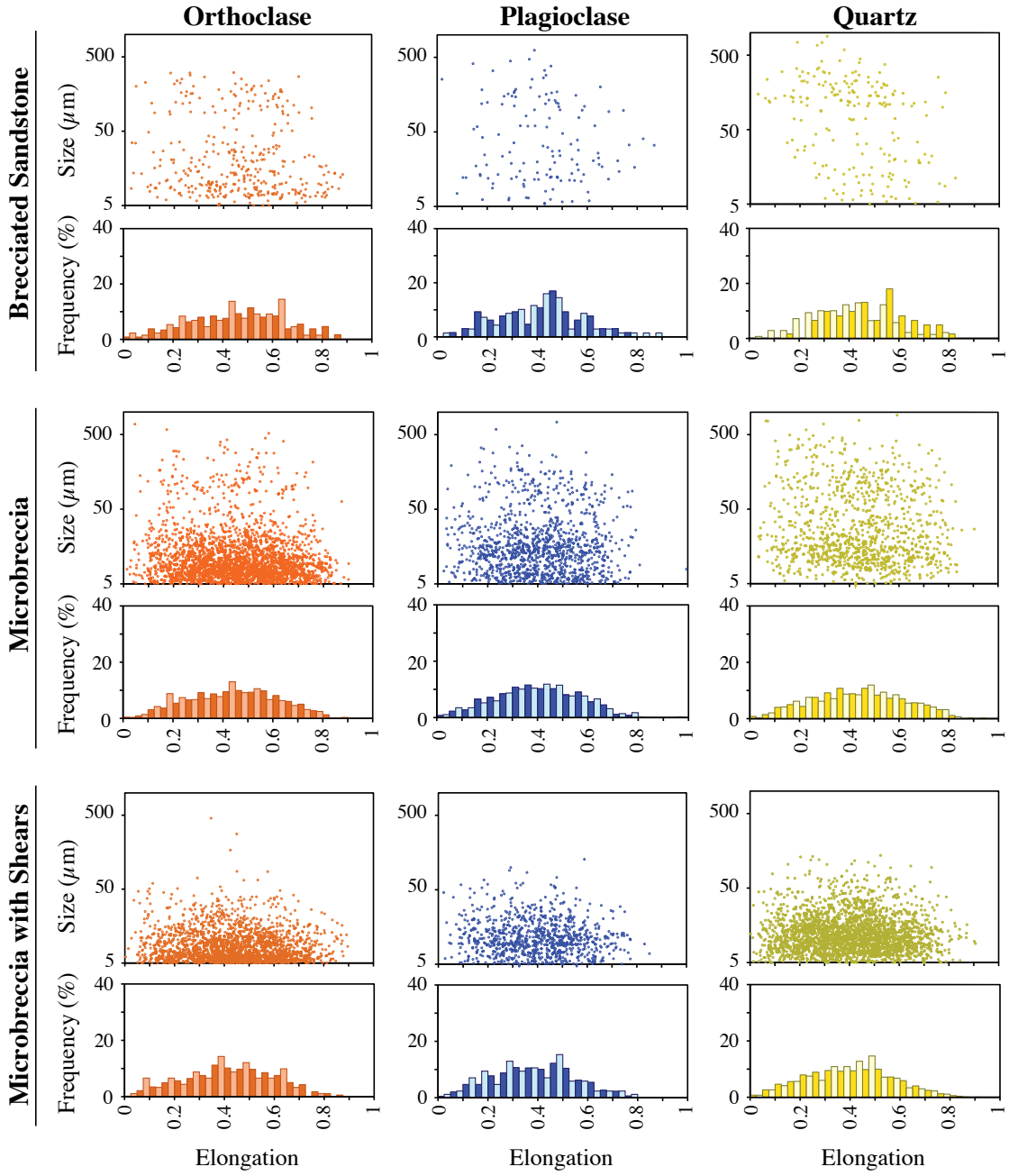

Figure 10. Continued

Table 3. Circularity Distribution Statistics by Mineral, Structural Unit, and Particle Size[a]

	Structural Unit	Particle Size Fraction	# of Data Points	Maximum	Minimum	Mean	Standard Deviation	Skewness	Kurtosis
Orthoclase	BSS	All	367	0.96	0.15	0.59	0.15	0.74	-0.96
		Small	236	0.96	0.15	0.60	0.17	0.32	-1.48
		Large	131	0.80	0.18	0.59	0.12	1.28	0.46
	MB	All	2520	1.00	0.11	0.59	0.16	0.38	-1.46
		Small	2236	1.00	0.17	0.59	0.16	0.34	-1.52
		Large	284	0.86	0.11	0.57	0.14	0.71	-0.81
	MBS	All	1966	1.00	0.06	0.59	0.18	0.14	-1.49
		Small	1876	1.00	0.13	0.60	0.18	0.13	-1.52
		Large	90	0.81	0.06	0.48	0.18	0.57	-0.33
Plagioclase	BSS	All	133	0.97	0.14	0.62	0.14	1.45	1.23
		Small	65	0.97	0.35	0.65	0.15	1.05	0.32
		Large	68	0.81	0.14	0.60	0.12	1.65	1.70
	MB	All	1139	0.96	0.13	0.62	0.15	0.79	-0.85
		Small	852	0.96	0.13	0.62	0.16	0.77	-0.84
		Large	287	0.87	0.19	0.60	0.13	0.83	-0.87
	MBS	All	871	0.93	0.18	0.62	0.14	0.71	-1.02
		Small	786	0.93	0.18	0.63	0.14	0.66	-1.16
		Large	85	0.87	0.21	0.58	0.15	1.62	2.12
Quartz	BSS	All	200	0.93	0.25	0.64	0.12	1.39	0.56
		Small	61	0.93	0.25	0.63	0.15	0.96	-0.79
		Large	139	0.87	0.3	0.65	0.11	1.52	1.06
	MB	All	1059	0.93	0.14	0.58	0.14	0.65	-1.18
		Small	623	0.93	0.14	0.58	0.14	0.58	-1.27
		Large	436	0.84	0.19	0.58	0.14	0.79	-0.82
	MBS	All	2422	1	0.13	0.6	0.16	0.52	-1.23
		Small	2156	1	0.13	0.61	0.16	0.51	-1.27
		Large	266	0.82	0.18	0.52	0.16	0.51	-1.04

[a]All refers to particles > 5 μm; Small refers to particles ranging from 5 to 25 μm; Large refers to particles > 25 μm

Table 4. Solidity Distribution Statistics by Mineral, Structural Unit, and Particle Size[a]

	Structural Unit	Particle Size Fraction	# of Data Points	Maximum	Minimum	Mean	Standard Deviation	Skewness	Kurtosis
Orthoclase	BSS	All	367	0.97	0.53	0.83	0.09	1.49	0.70
		Small	236	0.95	0.53	0.80	0.08	1.63	1.55
		Large	131	0.97	0.72	0.89	0.06	2.51	6.10
	MB	All	2520	0.97	0.50	0.81	0.08	1.81	2.11
		Small	2236	0.96	0.50	0.80	0.08	1.87	2.29
		Large	284	0.97	0.62	0.87	0.06	2.44	5.04
	MBS	All	1966	0.95	0.43	0.79	0.09	1.63	1.37
		Small	1876	0.95	0.43	0.79	0.09	1.62	1.30
		Large	90	0.95	0.65	0.84	0.07	2.33	5.26
Plagioclase	BSS	All	133	0.97	0.43	0.87	0.08	2.75	7.34
		Small	65	0.95	0.65	0.85	0.07	2.11	3.47
		Large	68	0.97	0.43	0.88	0.08	3.30	11.23
	MB	All	1139	0.98	0.20	0.85	0.07	2.11	3.42
		Small	852	0.98	0.42	0.84	0.08	2.04	3.24
		Large	287	0.96	0.61	0.88	0.06	2.64	6.08
	MBS	All	871	0.96	0.53	0.83	0.07	2.43	5.65
		Small	786	0.95	0.57	0.83	0.07	2.35	5.06
		Large	85	0.96	0.62	0.86	0.06	3.21	11.01
Quartz	BSS	All	200	0.98	0.6	0.88	0.07	2.46	5.88
		Small	61	0.93	0.6	0.81	0.07	2.33	5.4
		Large	139	0.98	0.71	0.91	0.05	3.2	11.08
	MB	All	1059	0.97	0.51	0.84	0.07	2.16	4.11
		Small	623	0.94	0.54	0.82	0.07	2.15	3.65
		Large	436	0.97	0.51	0.87	0.07	2.56	5.76
	MBS	All	2422	0.96	0.34	0.83	0.07	2.18	4.22
		Small	2156	0.96	0.34	0.83	0.07	2.19	4.26
		Large	266	0.95	0.58	0.85	0.07	2.21	4.13

[a]All refers to particles > 5 μm; Small refers to particles ranging from 5 to 25 μm; Large refers to particles > 25 μm

Table 5. Elongation Distribution Statistics by Mineral, Structural Unit, and Particle Size[a]

	Structural Unit	Particle Size Fraction	# of Data Points	Maximum	Minimum	Mean	Standard Deviation	Skewness	Kurtosis
Orthoclase	BSS	All	367	0.88	0.03	0.46	0.19	0.24	-1.21
		Small	236	0.88	0.03	0.47	0.19	0.14	-1.01
		Large	131	0.76	0.03	0.43	0.18	0.76	-0.25
	MB	All	2520	0.90	0.01	0.45	0.18	0.03	-1.63
		Small	2236	0.90	0.01	0.46	0.18	0.05	-1.65
		Large	284	0.87	0.05	0.42	0.18	0.29	-0.94
	MBS	All	1966	0.90	0.00	0.44	0.18	0.20	-1.34
		Small	1876	0.90	0.00	0.44	0.18	0.18	-1.36
		Large	90	0.75	0.04	0.39	0.17	0.54	-0.68
Plagioclase	BSS	All	133	0.87	0.02	0.42	0.17	0.93	0.23
		Small	65	0.79	/08	0.42	0.17	0.89	0.55
		Large	68	0.87	0.02	0.42	0.17	1.09	0.07
	MB	All	1139	0.99	0.02	0.40	0.16	0.24	-1.59
		Small	852	0.99	0.02	0.40	0.16	0.23	-1.63
		Large	287	0.79	0.04	0.40	0.17	0.34	-1.31
	MBS	All	871	0.85	0.02	0.4	0.16	0.36	-1.39
		Small	786	0.85	0.03	0.4	0.16	0.36	-1.45
		Large	85	0.75	0.02	0.37	0.16	0.8	-0.31
Quartz	BSS	All	200	0.82	0.03	0.42	0.17	0.39	-1.47
		Small	61	0.82	0.18	0.51	0.15	0.95	0.49
		Large	139	0.78	0.03	0.38	0.16	0.58	-1.26
	MB	All	1059	0.9	0.03	0.44	0.18	0.05	-1.26
		Small	623	0.83	0.03	0.4	0.18	0.1	-1.31
		Large	436	0.9	0.04	0.43	0.19	0.1	-1.1
	MBS	All	2422	0.91	0	0.4	0.17	0.11	-1.65
		Small	2156	0.91	0	0.4	0.18	0.06	-1.69
		Large	266	0.81	0.01	0.4	0.16	0.78	-0.4

[a]All refers to particles > 5 μm; Small refers to particles ranging from 5 to 25 μm; Large refers to particles > 25 μm

(a)

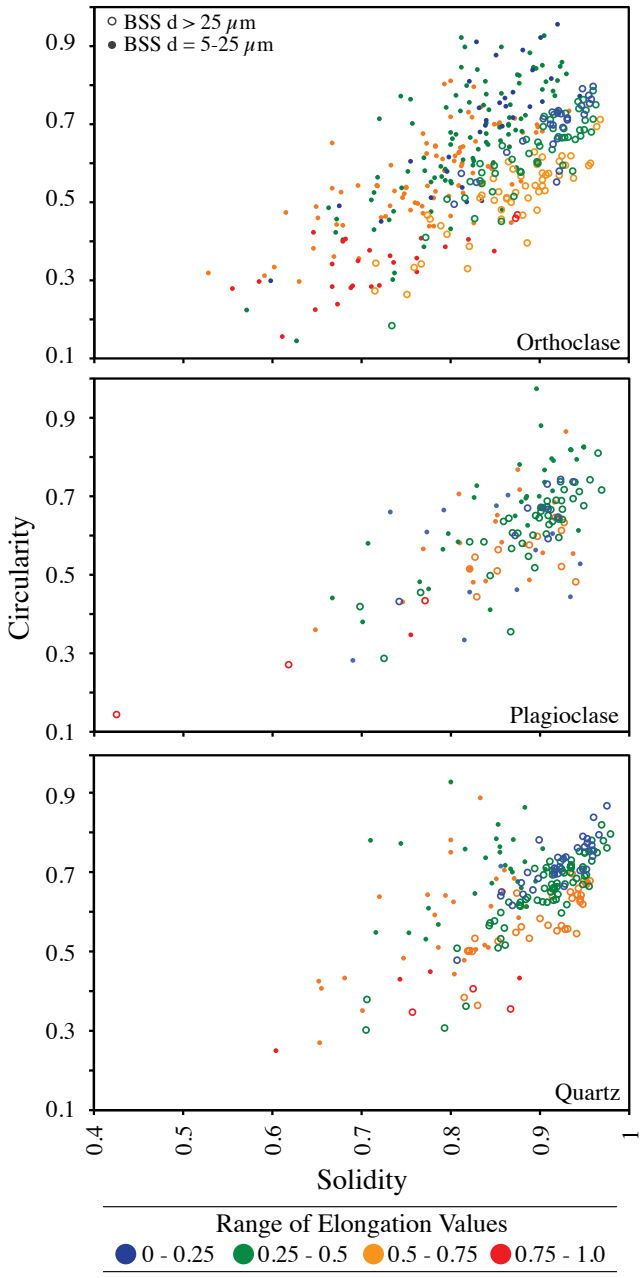

Figure 11. Cross plots showing the relationship between solidity, circularity, and elongation. Elongation values are binned and color-coded, where each color represents a specified range of elongation values. Plots show data for (a) two particle-size fractions in the BSS (5 to 25 μm and >25 μm) , and (b) particles from 5 to 25 μm in the MBS. In (a) the open circles distinguish the large size-fraction (> 25 μm) and the solid circles distinguish the small size-fraction (5 to 25 μm).

(b)

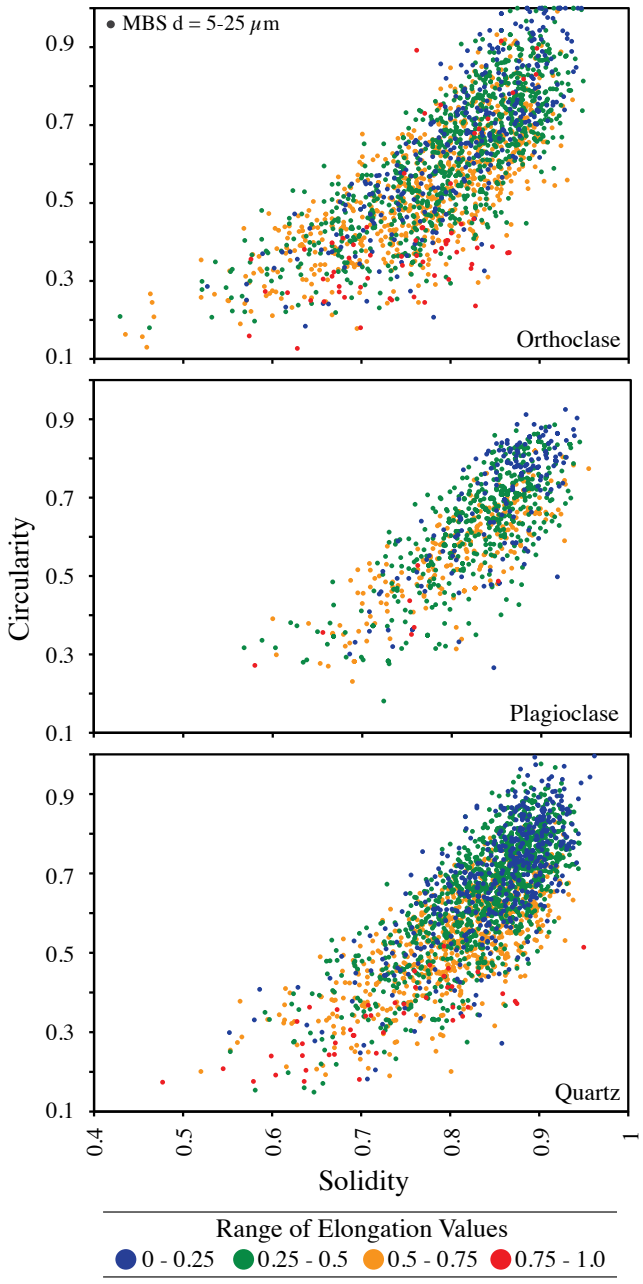

Figure 11. Continued

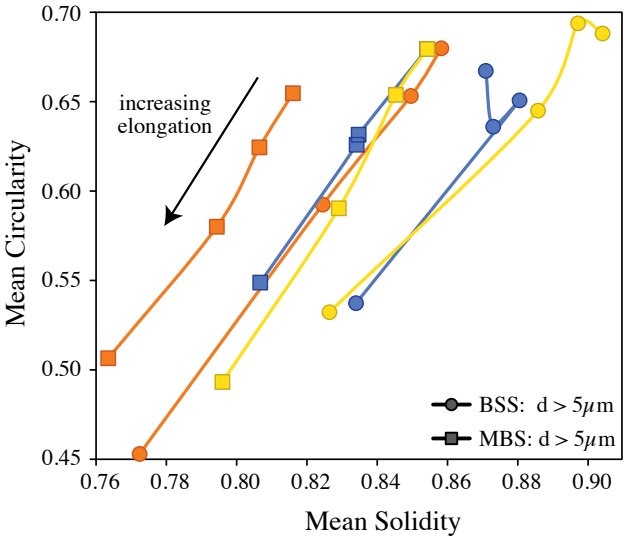

Figure 12. Mean circularity versus mean solidity for population quartiles based on elongation. Plot summarizes the solidity-circularity-elongation trends for different minerals and magnitudes of shear strain. The data points represent the shape data, after it has been sorted by elongation, and divided into four bins each containing an equal number of particles. Then, for each quartile, the means in circularity, solidity and elongation are calculated. Orthoclase is shown in orange, plagioclase in blue, and quartz in yellow.

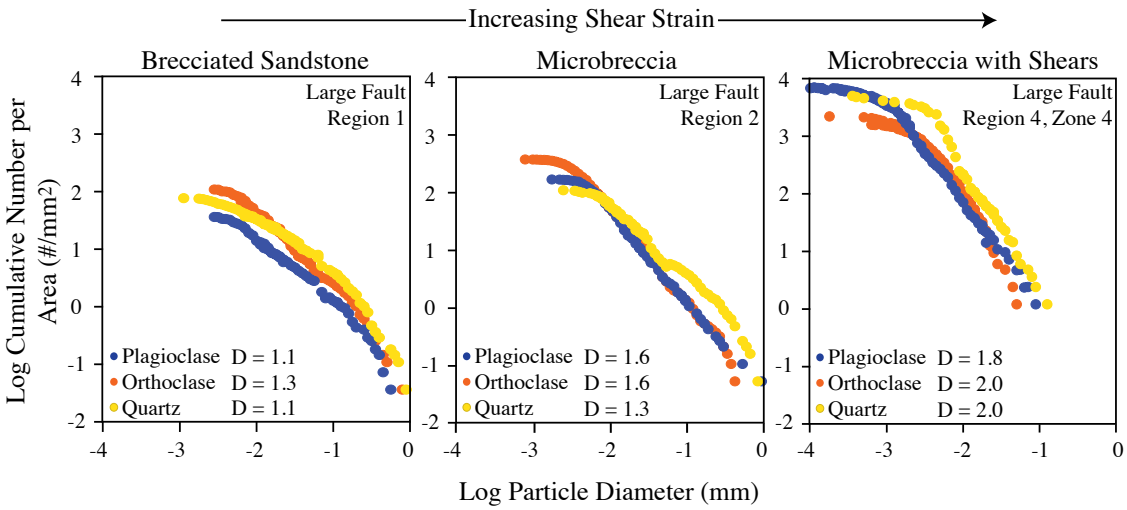

Figure 13. Composite PSD plots for orthoclase, plagioclase, and quartz for the three structural units of the large subsidiary fault. Data are plotted as log cumulative number per area versus log particle diameter in order of increasing shear strain. Data for all magnifications analyzed are combined for each mineral (see Figure 7 for details). The best-fit D is indicated.

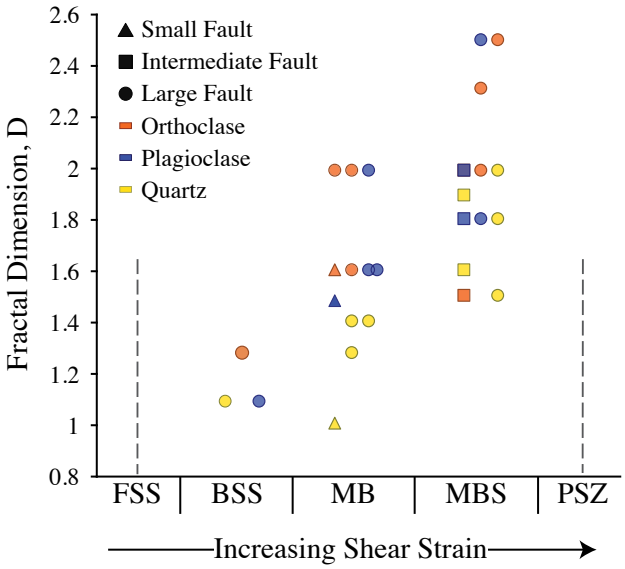

Figure 14. Plot of D as a function of shear strain, mineralogy, and fault size-class. The plot shows an increase in D with an increase in shear strain and smaller D for quartz compared to plagioclase and orthoclase. The dashed grey lines indicate structural units not described in this study (FSS and PSZ).

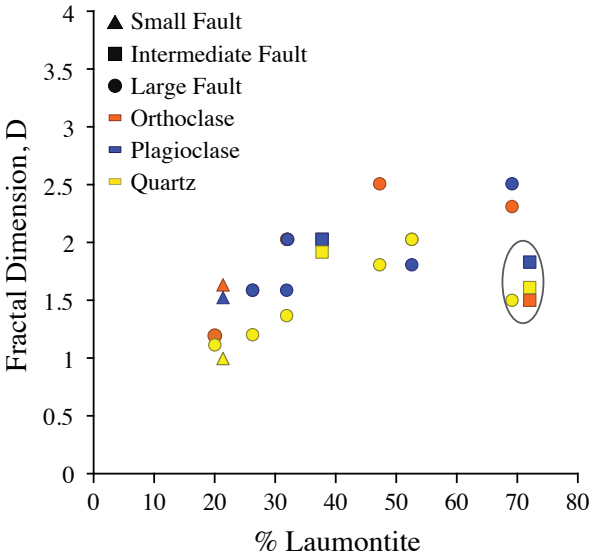

Figure 15. Plot of D versus area fraction of laumontite. The shape of the symbol defines the fault size-class, and the color of the symbol distinguishes the mineral phase. The circled points represent data from sheared dilatant veins; the squares represent data for Region 2 of the intermediate subsidiary fault, and the circle represents data for Region 4, Zone 3 of the large subsidiary fault.

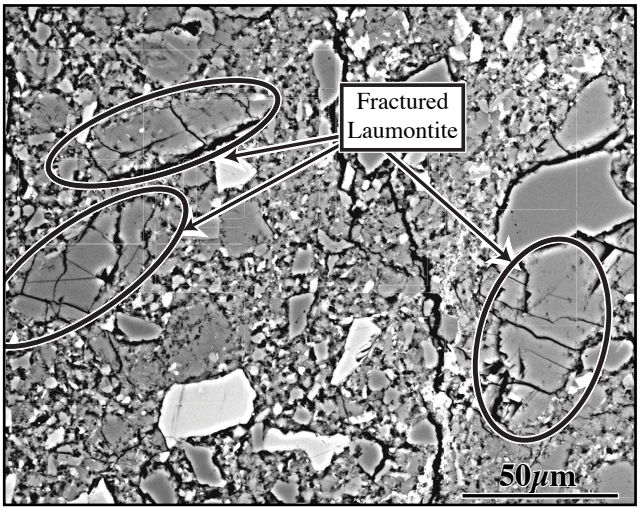

Figure 16. BSE image showing fractured laumontite particles in the large subsidiary fault (Region 4, Zone 4).

Table 6. Example Portion of the Spreadsheet Used to Interpret the Minerals Present in the Composite Element Maps

Pixel Gray Value	Numeric Combination	Element Combination	Mineral ID	Color	Composite Map Pixel Counts
0	0	none	Other	White	14
1	1	Mg			0
2	2	P			0
3	1+2	Mg+P			0
4	4	Al			5
5	1+4	Mg+Al			0
6	2+4	P+Al			0
7	3+4	3+Al			0
8	8	Fe	Fe oxides	Dk Brown	2
9	1+8	Mg+Fe			0
10	2+8	P+Fe			0
11	1+2+8	Mg+P+Fe			0
12	4+8	Al+Fe			5
13	1+4+8	Mg+Al+Fe			0
14	2+4+8	P+Al+Fe			0
15	1+2+4+8	Mg+P+Al+Fe			0
16	16	Si	Quartz	Lt Yellow	58127
17	1+16	Mg+Si			38
18	2+16	P+Si			0
19	1+2+16	Mg+P+Si			0
20	4+16	Al+Si	Al-Silicate	Lt Pink	3135

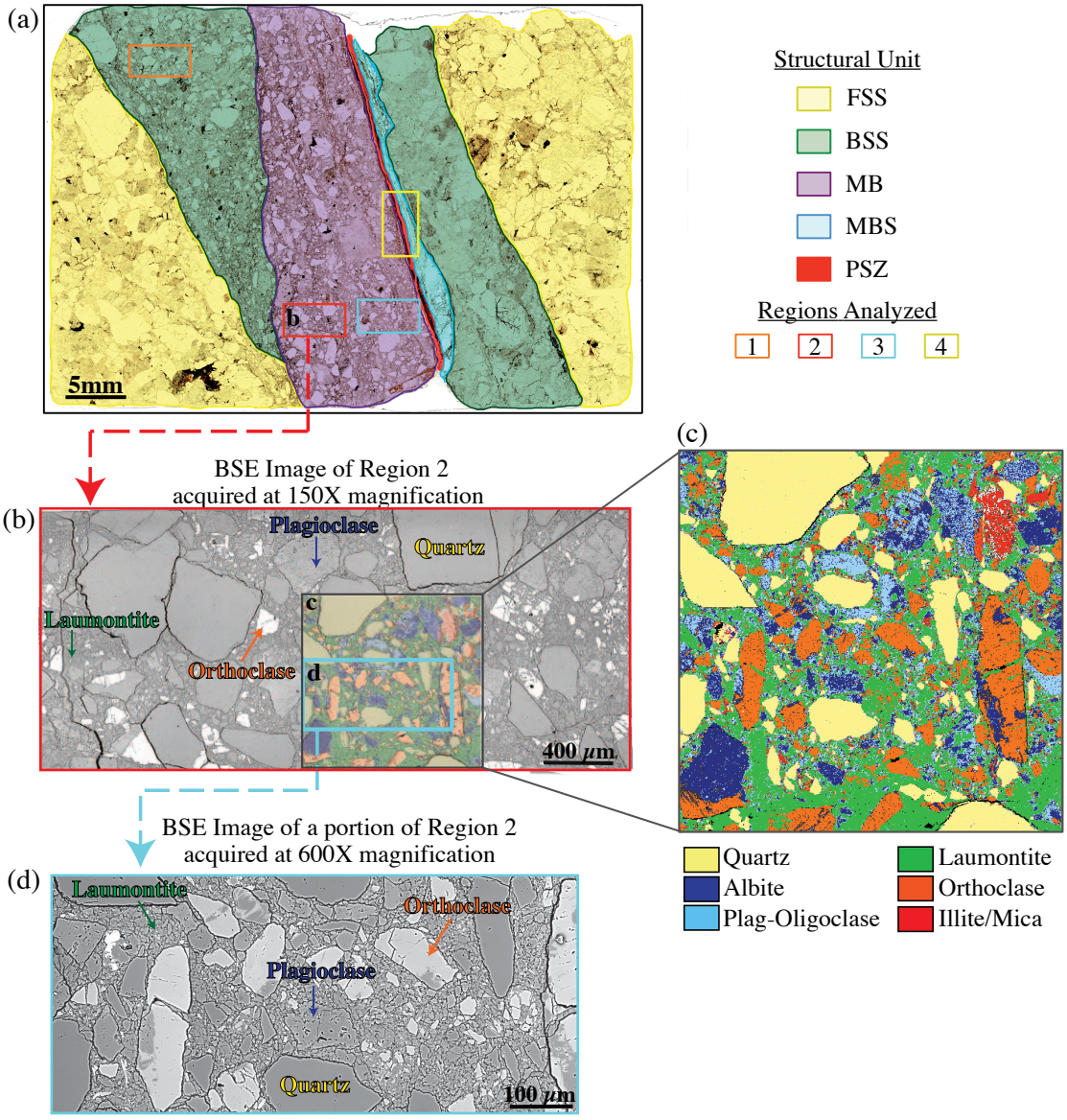

Figure 17. Plane light and BSE images, and composite element map shown for portions of the large subsidiary fault. (a) Plane light image showing the different structural units and four representative regions chosen for analysis BSE images and composite element map were taken in Region 2 (red box labeled b). (b) BSE image of Region 2 at higher magnification (acquired at 150X) showing gray-scale differences for the analyzed mineral phases and an example of a region analyzed by element mapping, shown in (c). (c) An example of a 1-mm^2 composite element map overlying a portion of the BSE image, shown in (b), to illustrate the type of image used to define mineral phases and particle outlines. (d) BSE image of a smaller portion of Region 2 acquired at 600X. To define mineral phases and particle outlines, this image would be underlain a composite element map.

Table 7. Portion of Spreadsheet used in PSD and Shape Analyses for Orthoclase from the MB (Region 2) of the Large Subsidiary Fault[a]

	A	B	C	D	E	F	G	H	I	J	K	L	M
1	A	d	A (μm)	d (um)	CN	log d	log CN	Perim	Major	Minor	Elong	Circ	Solid
2	11055	118.6	157422.6	447.7	1	2.65	0.00	488.17	180.37	78.04	0.57	0.58	0.92
3	9081	107.5	129312.9	405.8	2	2.61	0.30	580.40	179.13	64.55	0.64	0.34	0.62
4	8653	105.0	123218.2	396.1	3	2.60	0.48	419.75	134.14	82.13	0.39	0.62	0.91
5	5519	83.8	78590.2	316.3	4	2.50	0.60	338.39	120.37	58.38	0.52	0.61	0.91
6	4966	79.5	70715.6	300.1	5	2.48	0.70	331.56	88.91	71.11	0.20	0.57	0.87
7	4945	79.3	70416.5	299.4	6	2.48	0.78	322.69	89.27	70.53	0.21	0.60	0.85
8	4364	74.5	62143.1	281.3	7	2.45	0.85	384.38	118.16	47.03	0.60	0.37	0.67
9	2865	60.4	40797.4	227.9	8	2.36	0.90	239.91	65.69	55.53	0.15	0.63	0.86
10	2510	56.5	35742.3	213.3	9	2.33	0.95	263.97	114.90	27.81	0.76	0.45	0.93
11	1861	48.7	26500.5	183.7	10	2.26	1.00	192.79	73.62	32.19	0.56	0.63	0.90
12	1616	45.4	23011.7	171.2	11	2.23	1.04	188.89	50.97	40.37	0.21	0.57	0.85
13	1285	40.4	18298.3	152.6	12	2.18	1.08	163.78	56.82	28.80	0.49	0.60	0.92
14	1277	40.3	18184.4	152.2	13	2.18	1.11	184.41	65.40	24.86	0.62	0.47	0.80

[a]A, area; d, diameter; CN, cumulative number; Perim, perimenter; Elong, elongation; Circ, circularity; Solid; solidity

Table 8. Example Portion of the Normalization Spreadsheet Used to Bin and Area Shift the PSD Data and Create the Final Composite PSD Plots

<>	A	B	C	D	E	F	G	H	I	J
1	Global Variables		50X	Log d (μm)	Log CN	bin log d	bin log d (mm)	log norm #		
2				2.650989	0	2.65	-0.35	-1.26748	-0.35	-1.26748
3	Areas (mm^2)			2.608276	0.301	2.6	-0.4	-0.96645	-0.4	-0.96645
4	Macro	18.5130		2.597793	0.4771	2.55	-0.45	-0.79036	-0.45	-0.79036
5	995	0.9001		2.500139	0.6021	2.5	-0.5	-0.66542	-0.5	-0.66542
6	249	0.2549		2.477213	0.699	2.45	-0.55		-0.55	-0.48933
7	62.2	-		2.476292	0.7782	2.45	-0.55	-0.48933	-0.6	-0.42238
8	15.5	-		2.449152	0.8451	2.4	-0.6	-0.42238	-0.65	-0.36439
9	Area shift factor			2.357771	0.9031	2.35	-0.65	-0.36439	-0.7	-0.31323
10	Macro	1		2.329046	0.9542	2.3	-0.7	-0.31323	-0.75	-0.26748
11	995	0.26		2.264082	1	2.25	-0.75	-0.26748	-0.8	-0.22608
12	249	0.22		2.23343	1.0414	2.2	-0.8	-0.22608	-0.85	-0.12135
13	62.2	-		2.183661	1.0792	2.15	-0.85		-0.9	-0.0122
14	15.5	-		2.182305	1.1139	2.15	-0.85		-0.95	0.094251
15	Plot increment			2.166435	1.1461	2.15	-0.85	-0.12135	-1	0.147497
16	Log d =	0.05		2.133935	1.1761	2.1	-0.9		-1.05	0.209644
17				2.130292	1.2041	2.1	-0.9		-1.1	0.276591
18				2.10992	1.2304	2.1	-0.9		-1.15	0.323588

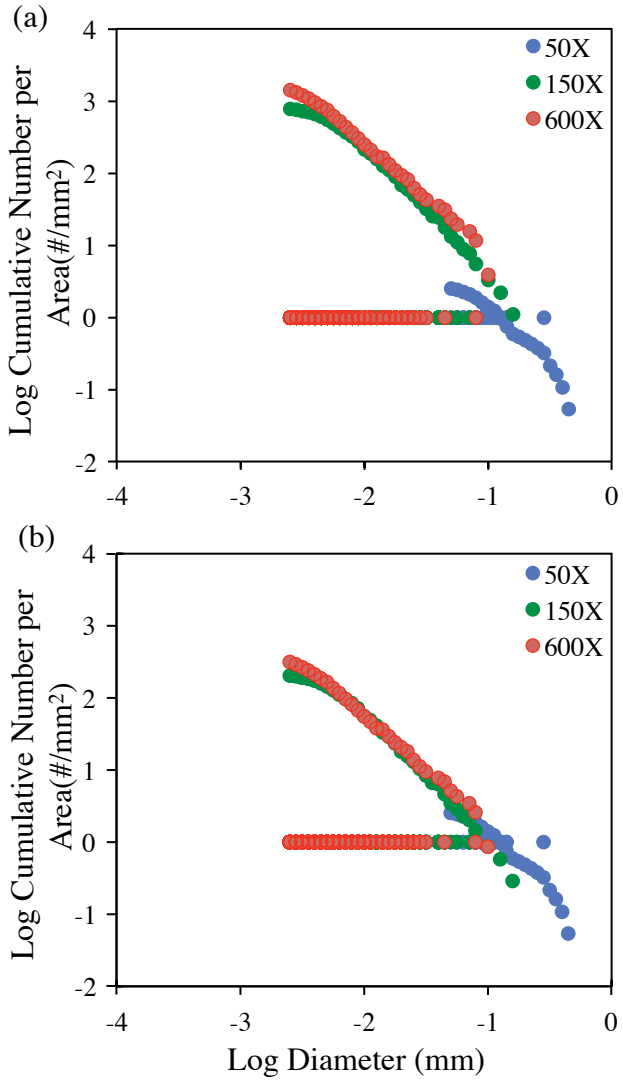

Figure 18. Example of composite PSD plots before and after the global variables – area shift factors are applied. Data are plotted as log cumulative number per area versus log particle diameter. Colors distinguish data collected at three magnifications. The cumulative number of particles recorded for each magnification is normalized by the area analyzed at that magnification. (a) Composite PSD plot prior to applying the area shift factors using the PSD normalization spreadsheet. (b) Composite PSD plot after applying area shift factors for 150X and 600X. The PSD data recorded for 150X (995 in *column A* of Table A2.2) is shifted 0.26 and the PSD data recorded for 600X (249 in *column A* of Table A2.2) is shifted 0.22. Data shown are for orthoclase from the MB (Region 2) of the large subsidiary fault.

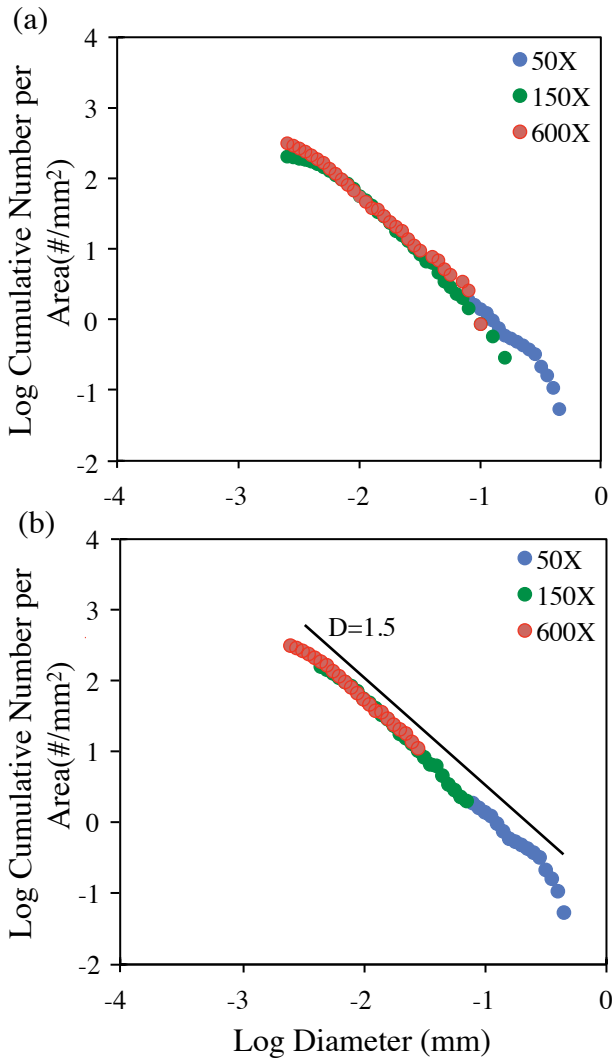

Figure 19. Example of composite PSD plots before and after the cut-offs have been defined for each magnification. Data are plotted as log cumulative number per area versus log particle diameter. Colors distinguish data collected at three magnifications. The cumulative number of particles recorded for each magnification is normalized by the area analyzed at that magnification. (a) Composite PSD plot before the cut-offs have been defined for each magnification. (b) Composite PSD plot after the cut-offs have been defined for each magnification. Slope of the best-fit line and D are shown. Data shown are for orthoclase from the MB (Region 2) of the large subsidiary fault.

VITA

Name:	Bretani Rebecca Heron
Address:	Anadarko Petroleum Corporation, 1201 Lake Robbins Drive, The Woodlands, TX 77380
Email Address:	bretani.heron@gmail.com
Education:	B.S., Geology, The University of Texas at Austin, 2008 M.S., Geology, Texas A&M University, 2011